

國立清華大學

物理系

碩士論文

角解析光電子能譜研究 TTC 於銀薄膜在鍺(111)基底
上之介面結構及量子井態之行為(初稿)

Studies of the interfacial structure and behavior of QWS for
a well-ordered ultrathin film of tetratetracontane ($n\text{-C}_{44}\text{H}_{90}$;
TTC)/Ag thin film/Ge(111) by ARPES

學 號： 9722539

研 究 生： 許哲嘉 (Che-Chia Hsu)

指導教授： 唐述中 博士 (Dr. Shu-Jung Tang)

中華民國百年二月

角解析光電子能譜研究 TTC 於銀薄膜在鍺(111) 基底上之介面結構及量子井態之行為

國立清華大學物理研究所碩士學位論文

題目：角解析光電子能譜研究 TTC 於銀薄膜在鍺(111)基底
上之介面結構及量子井態之行為

學生：許哲嘉

指導教授：唐述中 博士

摘要

我們利用角解析光電子能譜研究 tetratetracontane ($n\text{-C}_{44}\text{H}_{90}$; TTC)在銀薄膜上量子井態的行為。我們發現在鍍上 TTC 之後，量子井態 (Quantum-well state) 會往費米能階平移，而此趨勢與真空態 (Vacuum level) 的平移趨勢相符合。量子井態些許地向費米能階平移代表費米面所包圍的面積縮小，亦即電子態密度減小。對於研究量子井態的行為更能夠合理地解釋電子在介面的行為，由於量子井態的波函數束縛在金屬薄膜內並不會受到有機薄膜的破壞，而所量測到的真空態平移為 -0.62 eV 。我們提出一個模型來解釋此介面的機制，根據量子井態的變化以及真空態的平移，mirror force 支配著介面的電荷分布，我們假設像電荷效應 (Image charge effect) 發生在此介面。此外，我們也得到分子軌域的能帶色散 (Energy band dispersion)，我們觀察到分子內 (Intra-molecular) 以及分子間 (Inter-molecular) 能帶色散，與之前 Ishii 團隊所量測以及計算的相符合。此外，額外的能帶色散我們推測是由於 TTC 分子由於鍺基底的三軸對稱 (Three-fold symmetry) 而作 60° 度角的排列而得到。

Studies of the interfacial structure and behavior of quantum-well-state (QWS) for a well-ordered ultrathin film of tetratetracontane (n-C₄₄H₉₀; TTC)/Ag thin film/Ge(111) by Angle-resolved photoemission spectroscopy (AR-UPS)

Master Degree in Department of Physics and Astronomy,

National Tsing Hua University, Hsin-Chu, Taiwan

Student: Che-Chia Hsu

Advisor: Prof. Shu-Jung Tang

Abstract

We have investigated the quantum-well-state (QWS) behavior of Ag thin film with tetratetracontane (n-C₄₄H₉₀; TTC) deposited on top by angled-resolved photoemission spectroscopy (AR-PES). We found that QWS shift towards Fermi level and the trend is consistent with vacuum level (VL) shifts. The slight shift of QWS towards Fermi level means that the area of the Fermi surface enclosed by the QWS bands shrinks and consequently the occupied charge density should decrease. It is more reasonable to discuss the charge behaviors at the interface by the investigation of the behaviors of QWS. As the wave functions of QWS are confined within the metal film, they will not be destroyed after the deposition of organic thin films. We had measured the VL shift Δ , which is about - 0.62 eV. We bring up a model to explain the mechanism at the interface. According to the results of QWS change and VL shift, the mirror force seems to dominate the charge distribution and we can speculate that the image charge effect takes place at the interface. We also obtained the energy band dispersion of the occupied molecular orbital state. Both the inter-molecular and the intra-molecular band dispersions were observed, which are consistent with the previous calculated and measured results by Ishii et al. However, extra energy band dispersions were also observed possibly due to the TTC molecules aligning 60 degrees with the others as a result of three-fold symmetry of the Ge(111) symmetry.

Contents

1	Introduction	3
2	Background Theory	5
2.1	Surface and Interface	5
2.1.1	Introduction	5
2.1.2	Two-dimensional Lattice and Reciprocal Space	6
2.2	Photoemission Spectroscopy (PES)	10
2.2.1	Introduction	10
2.2.2	Photoemission Process	11
2.2.3	Three-step Model	12
2.2.4	Angle-Resolved Photoemission Spectroscopy (AR-PES)	18
2.3	Electronic States	18
2.3.1	Surface State	18
2.3.2	Quantum Well State	21
2.3.3	Electronic Structure of an Organic Solid	22
2.4	Organic Material	26
2.4.1	Interfacial Dipole and Energy Level Alignment	26
2.4.2	Tetratetracontane (TTC)	28
3	Experimental Instruments and Techniques	30
3.1	Instrumental Setup and Experimental Process	30
3.1.1	Instrument Setup	30
3.1.2	Sample Preparation	31
3.1.3	Deposition of the Silver Films and TTC Films	33
3.2	Ultra-high Vacuum(UHV) Technology	35

3.2.1	Fundamental concept of UHV techniques	35
3.2.2	UHV Instruments and Procedures	36
3.3	Hemispherical Energy Analyzer	38
3.3.1	Introduction	38
3.3.2	Analyzer Modes	41
3.3.3	Energy Resolution	41
3.4	Residual Gas Analyzer (RGA)	43
3.4.1	Introduction	43
3.4.2	Conformation and Principle of RGA	44
3.5	Low-Energy Electron Diffraction (LEED)	47
3.5.1	Introduction and The Kinematic Theory of Low-Energy Elec- tron Diffraction	47
3.5.2	Conformation and Operation of LEED	48
3.6	Synchrotron Light Source	50
3.6.1	Introduction of Synchrotron Radiation	50
3.6.2	Beam-line Specifications	51
4	Well-ordered Ultrathin Film of Tetratetracontane (n-C₄₄H₉₀; TTC)/Ag thin film/Ge(111)	53
4.1	Electronic Structure and Molecular Orientation	53
4.2	Band Dispersion	56
4.3	QWS Change	59
4.3.1	Analytic Methods	59
4.3.2	Results and Discussions	61
4.4	Vacuum Level Shift	65
4.4.1	Experiment and Analytic Methods	65
4.4.2	Results and Comparison	66
4.4.3	Coupling between QWS change and VL shift	67
4.5	Model	67

Chapter 1

Introduction

Technology of electronic device has been widely developed for several decades. As the scale decreasing to nanometer, many physical properties will remarkably change due to the quantum-size effects (QSE). In recent years, many investigations have revealed that the physical properties depend strongly on the film thickness.[1, 2, 3, 4]

In addition, electronically functional organic materials have also attracted much attention for many years, especially for an organic electroluminescent (EL) device.[5] In order to understand and improve the performance of the device, to realize the interfacial electronic structure is an important task.

In previous reports, the systems of organic-on-metal (Org./Metal) interfaces were studied widely. The fact of the formation of interfacial dipole at the interface has been confirmed and established by H. Ishii in 1999.[5] However, these researches referred to only organic films deposited on metal substrate or opposite. Considering the applications in devices which are combinations of organic material and metal thin film, it is an interesting issue and worthy to be studied deeply in the future.

As a result of the study for a simple system with a well-ordered structure is highly desired. The possibility of chemical interaction at the interface should be avoided. Long chain alkane is a model oligomer of polyethylene which is one of the basic compounds in polymer science.[6] Additionally, the electronic structure of tetratetracontane (TTC: $n\text{-CH}_3(\text{CH}_2)_{42}\text{CH}_3$)/metal has been investigated widely for many

years. So that, we start from the system of TTC/Ag films/Ge(111). This work was performed at a 6m low-energy spherical grating monochromator (6m-LSGM) beamline (BL-08A) in NSRRC, Taiwan, and studied mainly by Angle-resolved photoemission spectroscopy (AR-PES), which is a powerful tool to directly probe the band structure.

Chapter 2 has the background theory including the lattice structure, AR-PES, the electronic states, and the organic material, especially for TTC. The experimental instruments and techniques used in this thesis will be introduced in Chapter 3. Chapter 4 exhibits some measurements and results of TTC/Ag films/Ge(111) system. We can observed the quantum-well states (QWS) change and vacuum level (VL) shift after the deposition of TTC film. The inter- and intra-molecular band dispersion of TTC will be compared with previous work. After that, we can bring up a model in this system. Finally, the conclusions in this thesis will be summarized in Chapter 5.



Chapter 2

Background Theory

2.1 Surface and Interface

2.1.1 Introduction

Unlike a bulk, a surface is regarded as some defects of the solid, and also revealed many different physics properties. The outmost atomic layers significantly differ from the bulk due to the creation of a surface would leave unsaturated bonds dangling into space, and these bonds are also called *dangling bonds*. Fig. 2.1(a) schematically illustrates that the absence of neighboring atoms on one side forms a surface which consists of a great deal of the dangling bonds. In order to reduce the energy, the position of atoms will slightly change to approach or leave each other and form bonds with their otherwise unused valence electrons, and then the interatomic forces in the uppermost lattice planes are considerably changed.[7]

There are two significant kinds of the characteristic rearrangements displayed in Fig. 2.1(b), (c), which defined *relaxation* and *reconstructure*, respectively. The pure compression (or extension) of the topmost (or top few) interlayer separations normal to the surface is called relaxation, as shown in Fig. 2.1(b). On the contrary, if the shifted atoms are toward the direction which is parallel with the surface plane, changing the periodicity which is parallel to the surface, this type of atomic rearrangement is then called reconstructure, as shown in Fig. 2.1(c).

As a result the displacement of the atomic position on the surface must be more

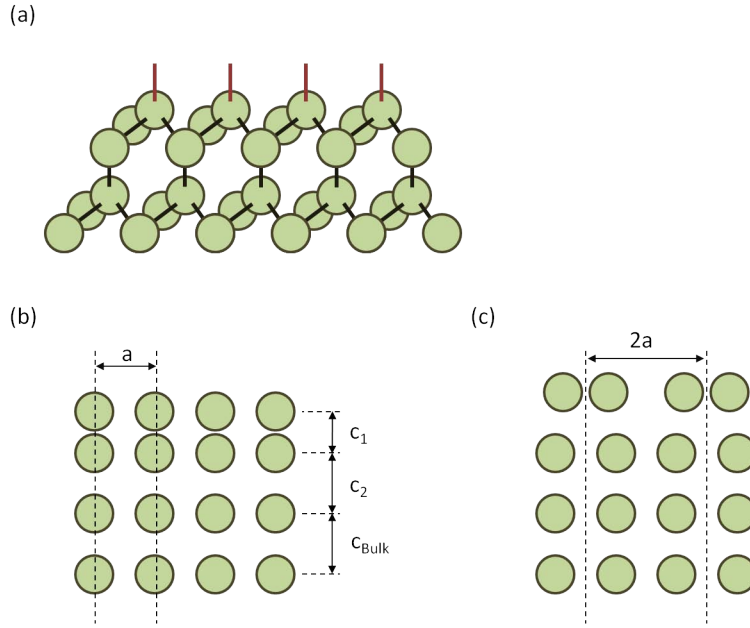


Figure 2.1: (a) Breaking symmetry of the solid and forming the dangling bonds (red lines) in the vacuum side. (b) The topmost layer slightly shift along the direction *normal* to the surface. This kind of rearrangement is called relaxation. (c) A reconstructure of the topmost atomic layer into a surface net with double periodicity distance $2a$.

complex than a pure shift. The experimental instruments which are used to determine the atomic position will be briefly introduced in later section, for example, low-energy electron diffraction (LEED) (Sec. 3.5), and angle-resolved ultraviolet photoemission spectroscopy (AR-UPS) (Sec. 2.2.1).

In terms of the atomic structure, the solid/solid interface might have different configurations such as those described in Fig. 2.2, and these can be classified into two groups, abrupt and non-abrupt interfaces, according to their molecular properties. Fig. 2.2(a) and Fig. 2.2(b) show the crystalline/crystalline and the amorphous/crystalline configurations, respectively. The abruptness of an interface might also be washed out by interdiffusion, as shown in Fig. 2.2(c), or formation of new chemical compounds, as shown in Fig. 2.2(d).

2.1.2 Two-dimensional Lattice and Reciprocal Space

Comparing with three-dimensional (3D) case, what we considered is two-dimensional (2D) point groups and 2-D Bravais lattices. As a result of the broken symmetry of

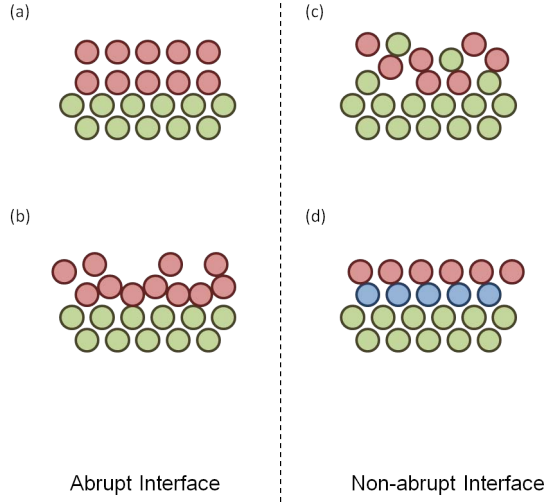


Figure 2.2: Different manner of the solid/solid interface. (a) crystalline/crystalline (b) amorphous/crystalline (c) interdiffusion (d) reaction of these two materials, and forming a new compound.

surface, all symmetry properties are 2D. The basic substrate lattice can be described by a set of 2D translational vectors

$$\mathbf{r}_{\mathbf{m}} = \alpha \mathbf{a}_1 + \beta \mathbf{a}_2 \quad (2.1)$$

where $\mathbf{m} = (\alpha, \beta)$ represent a pair of integer numbers, and $\mathbf{a}_1, \mathbf{a}_2$ are two unit vectors of the Bravais lattice. Afterwards, we can determine the surface net of the topmost atomic layer in terms of the substrate net by

$$\mathbf{b}_1 = \gamma_{11} \mathbf{a}_1 + \gamma_{12} \mathbf{a}_2 \quad (2.2)$$

$$\mathbf{b}_2 = \gamma_{21} \mathbf{a}_1 + \gamma_{22} \mathbf{a}_2 \quad (2.3)$$

Now, we can define the translational vectors of the 2D reciprocal lattice, \mathbf{a}_i^* , in terms of the real-space lattice vectors \mathbf{a}_i by

$$\mathbf{a}_1^* = 2\pi \frac{\mathbf{a}_2 \times \hat{\mathbf{n}}}{|\mathbf{a}_1 \times \mathbf{a}_2|} \quad (2.4)$$

$$\mathbf{a}_2^* = 2\pi \frac{\hat{\mathbf{n}} \times \mathbf{a}_1}{|\mathbf{a}_1 \times \mathbf{a}_2|} \quad (2.5)$$

Similar to the real-space relations, the reciprocal network of a superstructure, \mathbf{b}_1^* (\mathbf{b}_2^*) can be expressed in terms of the substrate reciprocal space \mathbf{a}_1^* (\mathbf{a}_2^*) by

$$\mathbf{b}_1^* = \gamma_{11}^* \mathbf{a}_1^* + \gamma_{12}^* \mathbf{a}_2^* \quad (2.6)$$

$$\mathbf{b}_2^* = \gamma_{21}^* \mathbf{a}_1^* + \gamma_{22}^* \mathbf{a}_2^* \quad (2.7)$$

For example, the sample which we used as a substrate in this experiment is Ge (111), so we briefly describe the structure and surface configurations here. The semiconductor Ge is a diamond structure crystal with lattice constant $a = 5.658 \text{ \AA}$. Considering the (111) direction, the STM image of a clean Ge (111) was performed by several groups and the results were shown in Fig. 2.3.[11, 12] The $c(2 \times 8)$ structure consists of two domains which are (2×2) and $c(2 \times 4)$ subunit cells. These domains result in two types of rest atoms (R_R, R_T) and adatoms (A_R, A_T) with different local environments as shown in Fig. 2.3(c), where the parallelogram represent a unit cell of $c(2 \times 8)$ structure. Fig. 3.4 shows the LEED patterns of Ge(111)- $c(2 \times 8)$ structure.

In order to realize the spectrum of our measurement, we should briefly introduce the surface Brillouin zone (SBZ) for a FCC crystal of the (111) direction, as schematically shown in Fig. 2.5. Fig. 2.5(a) shows the projection of bulk zone onto SBZ. Fig. 2.5(b) and (c) are cut through the bulk Brillouin zone in two directions of the SBZ, where k_{\parallel} and k_{\perp} are the wave vector parallel and perpendicular to the surface, respectively.[23]

According to these schemes, we can deduce the formula of distance from the zone center (Γ) to the zone boundary in two high-symmetry points for the (111) face of an FCC crystal, with

$$\bar{\Gamma}\bar{K} = \frac{\sqrt{2\pi}}{a \cos^2 30^\circ} \quad (2.8)$$

$$\bar{\Gamma}\bar{M} = \frac{\sqrt{2\pi}}{a \cos 30^\circ} \quad (2.9)$$

where a is the lattice constant.

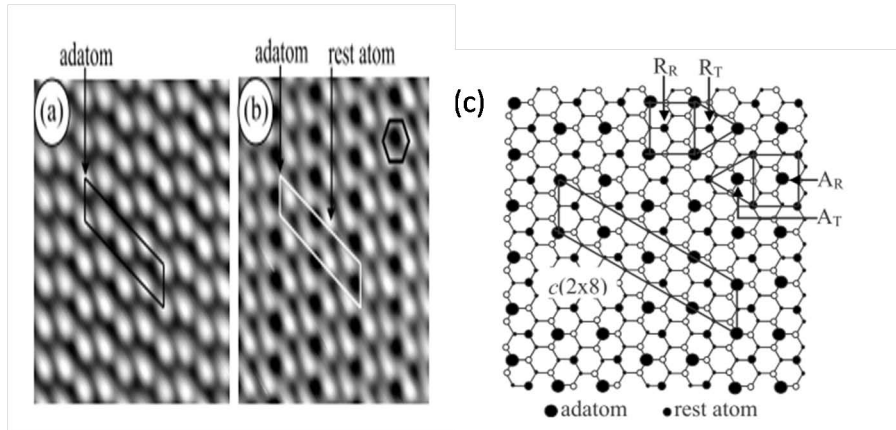


Figure 2.3: STM images of the clean Ge (111) $c(2 \times 8)$ structure and the atomic model. (a) Only adatoms were imaged. (b) Adatoms and rest atoms were imaged. (c) Atomic model of clean Ge (111) $c(2 \times 8)$ structure. One kind of rest atoms (adatoms) is symmetrically surrounded by three adatoms (rest atoms), and the other is asymmetrically surrounded by four adatoms (rest atoms).

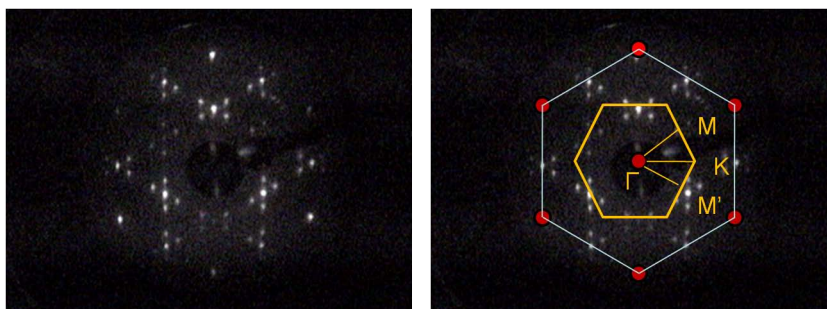
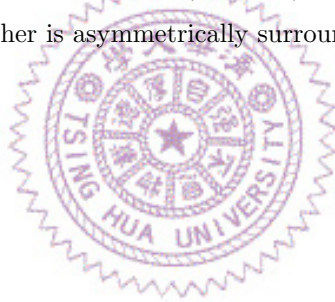


Figure 2.4: LEED pattern for a clean Ge (111) $c2 \times 8$ surface, and the applied electron energy is 35 eV.

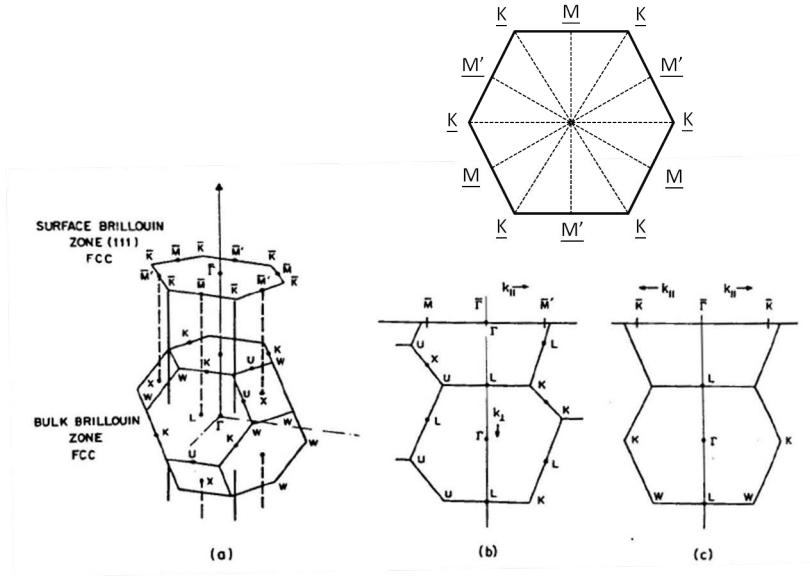


Figure 2.5: Surface Brillouin zone (SBZ) compared with the bulk Brillouin zone for a (111) direction of FCC crystal. Left illustration is the projection of a SBZ along (111) direction, and the corresponding SBZ is labeled on the right hand side.

2.2 Photoemission Spectroscopy (PES)

2.2.1 Introduction

In 1887, Heinrich Hertz was the first one who observed the phenomenon of photoelectric effect.[10] In 1905, Albert Einstein brought up an idea, which explained the effect as a quantum behavior governed by the relationship

$$E_{kin,max} = h\nu - \phi \quad (2.10)$$

among the maximum kinetic energy $E_{kin,max}$ of the photoelectrons, the photon energy $h\nu$, and the work function ϕ of the emitting solid.[9][19] It means that an electron absorbs the photon energy if it is sufficiently enough, and it will escape from the metal with finite kinetic energy.

This significant observation had indeed influenced the future science development profoundly. For instance, Photoelectron Spectroscopy (PES) is one of the important experimental techniques which is based on the photoelectric effect theory, and it is also called Photoemission Spectroscopy, too. The principle experimental

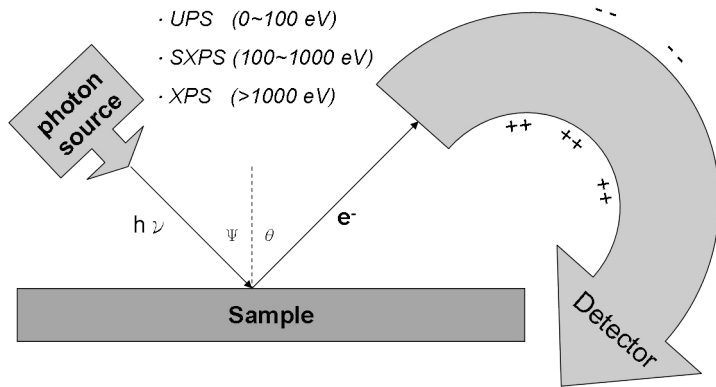


Figure 2.6: Sketch of a modern PES experiment. PES can be divided into different regions, depending on the incoming photon energy. (1) Ultra-violet photoelectron spectroscopy (UPS). (2) Soft X-ray photoelectron spectroscopy. (SXPS)(3) X-ray photoelectron spectroscopy. (XPS)[9]

measurement in this thesis is performed by using Angle-Resolved Photoemission Spectroscopy (AR-PES), which takes into account the emission angle of the photoelectrons. We will particularly introduce it in later section.

Nowadays, there are many different light sources and photon energy which can be used for different research targets. Fig. 2.6 exhibits the lay-out of modern Photoemission experiment, and the light source is either a gas-discharged lamp, an X-ray tube, or a synchrotron-radiation source. In this thesis, all of the experiment was performed by using of synchrotron-radiation source.

2.2.2 Photoemission Process

As shown in Fig. 2.6, the light (photon) impinges on the sample and the electrons are excited through the photoelectric effect. When the electrons are excited from an initial state of binding energy E_B by the photon with energy $h\nu$, it should overcome the work function of solid ϕ_{sample} and the remaining energy will be the kinetic energy of photon electrons. In other words, we can determine the binding energy E_B of the electrons in the sample from the following equation:

$$E_{kin,max} = h\nu - \phi - |E_B| \quad (2.11)$$

where the binding energy of an energy level measured by PES in solids is typically referenced to the sample Fermi level (E_F), and in free atoms or molecules to the vacuum level (VL).

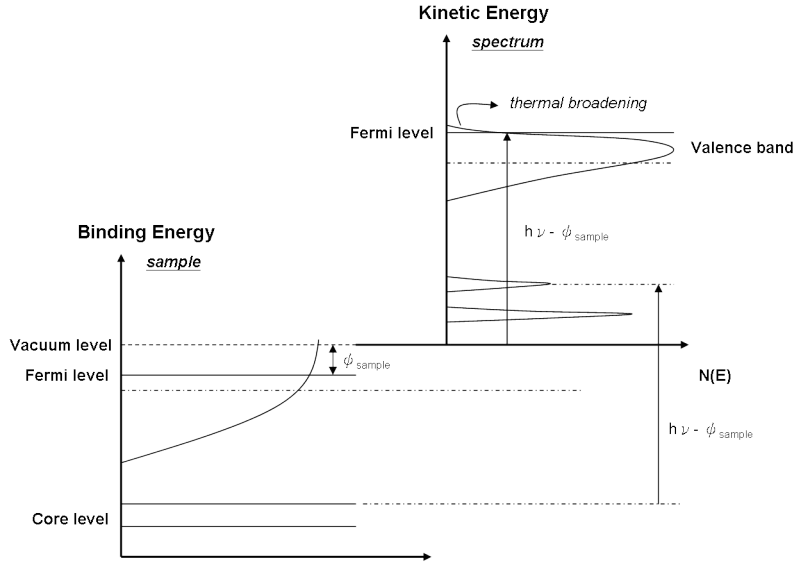


Figure 2.7: Schematic depiction of photoemission process and the relation between energy levels in a solid and energy distribution produced by photons of energy $h\nu$. [9]

Fig. 2.7 illustrates the photoemission process. The valence electrons in the sample are located within the continuous valence energy bands. When the kinetic energy of excited electrons exceeds the VL, these electrons will escape the sample. In actual data accumulation, notice that the photoelectron intensity extends a little above the Fermi level as a result of thermal broadening.

In addition, one should comprehend that the kinetic energy of the photoelectron is not detected in vacuum, but rather in an energy analyzer. Actually, the sample and the analyzer always do not have identical work functions so that these two kinetic energies are not equivalent. Fig. 2.8 shows the difference of work function between the sample and the analyzer, and describes the relationship between different energy characteristics. Φ_0 and Φ_{sp} are work functions of the specimen and the spectrometer, respectively. Considering the accurate measurement of the binding energy, we always ground both of the sample and the analyzer in order to align equivalently their Fermi level.

2.2.3 Three-step Model

After briefly introducing the photoemission process in last section, there is a typical model which divides the complicated photoemission process into three steps,

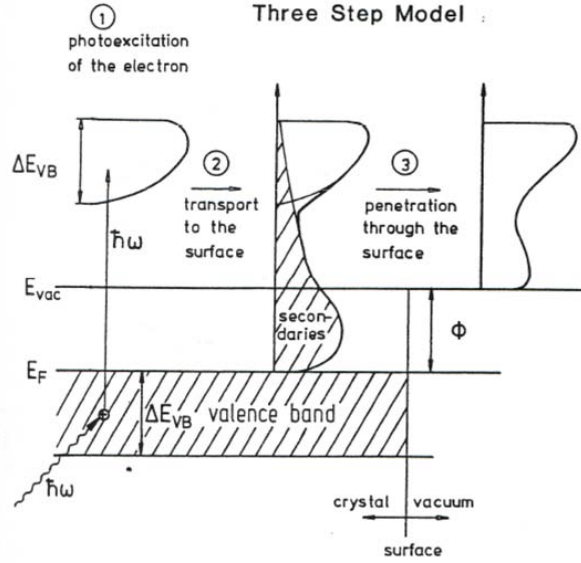


Figure 2.9: Pictorial representation of the three-step model description of the photoemission process.[9]

$$H_0\psi = -\frac{\hbar^2}{2m}\nabla^2\psi + V(\mathbf{r})\psi \quad (2.13)$$

$$H_{int}\psi = \frac{1}{2m}\left[-\frac{2e\hbar}{ic}\mathbf{A}\cdot\nabla\psi - \frac{e\hbar}{ic}(\nabla\cdot\mathbf{A})\psi + \frac{e^2}{c^2}|\mathbf{A}|^2\psi\right] \quad (2.14)$$

Here we can neglect the last term of Eq. 2.14 if the electromagnetic field strength is not too large. Considering the second term in Eq. 2.14, even though this term is small inside the crystal since \mathbf{A} is varying slowly in space, it can become relevant in the surface due to the presence of the surface potential which breaks the translation symmetry. However, we also neglect this effect in following description of photoemission.

When the light illuminates the sample, the electron is excited from initial state to final state. This process must obey the Fermi Golden Rule in first order time-dependent perturbation theory as described below

$$W_{fi} = \frac{2\pi}{\hbar} |\langle f, \mathbf{k} | H'_{int} | i, \mathbf{k} \rangle|^2 \delta(E_f(\mathbf{k}) - E_i(\mathbf{k}) - \hbar\omega) = m_{fi} \delta(E_f(\mathbf{k}) - E_i(\mathbf{k}) - \hbar\omega) \quad (2.15)$$

$$m_{fi} = \frac{2\pi}{\hbar} |\langle f, \mathbf{k} | H'_{int} | i, \mathbf{k} \rangle|^2 \quad (2.16)$$

where m_{fi} is a matrix element. $|i, \mathbf{k}\rangle$ and $|f, \mathbf{k}\rangle$ are the Bloch initial and final state in the solid, and E_i, E_f are the eigenvalues of H_0 , respectively. H'_{int} is an approximate perturbation operator. The delta-function describes the energy conservation in the excitation of an electron from an initial state into a final state of the electronic band structure.

Applying the momentum operator $\mathbf{p} = i\hbar\nabla$ to Eq. 2.16, we can obtain an equation described below

$$m_{fi} = \frac{2\pi}{\hbar} \frac{e^2}{m^2 c^2} |\mathbf{A} \cdot \langle f | \mathbf{p} | i \rangle|^2 = \frac{2\pi}{\hbar} \frac{e^2}{m^2 c^2} |\mathbf{A} \cdot \mathbf{P}_{fi}| \quad (2.17)$$

where \mathbf{P}_{fi} is the so-called momentum matrix element.

Considering the conservation of wave vectors as a result of elastic electron diffraction in photoemission process, the relationship is described as

$$\mathbf{k}_f = \mathbf{k}_i + \mathbf{k}_{photon} + \mathbf{G} \quad (2.18)$$

where \mathbf{G} is a reciprocal lattice vector of the bulk, and \mathbf{k}_{photon} is the wave vector of photon, which is commonly neglected in UPS regime. Accordingly, the internal electron current density is given by

$$I^{internal}(E, \hbar\omega, \mathbf{k}) \propto \sum_{f,i,\mathbf{G}} m_{fi} f(E_i) \delta(E_f(\mathbf{k}) - E_i(\mathbf{k}) - \hbar\omega) \cdot \delta(\mathbf{k}_f - \mathbf{k}_i - \mathbf{G}) \quad (2.19)$$

where $f(E_i)$ is the Fermi distribution function (E_i is occupied).[8]

Step2. Propagation of the photoexcited electron to the surface.

The large amounts of photoexcited electrons will undergo a series of inelastic scattering process which induced by electron-plasmon or electron-phonon effect during their propagation in a crystal. These inelastic scattering electrons contribute to the continuous background in photoemission spectrum which is called *True Secondary Background*. On the other hand, the electrons without inelastic scattering will arrive in the surface. The probability of these inelastic electrons is given phenomenologically by the mean-free-path λ , which will be introduced particularly in the section later. These photoelectrons which reach the surface can be characterized as a simplifivative coefficient $D(E, \mathbf{k})$, and it is also called the *transport probability*: [8]

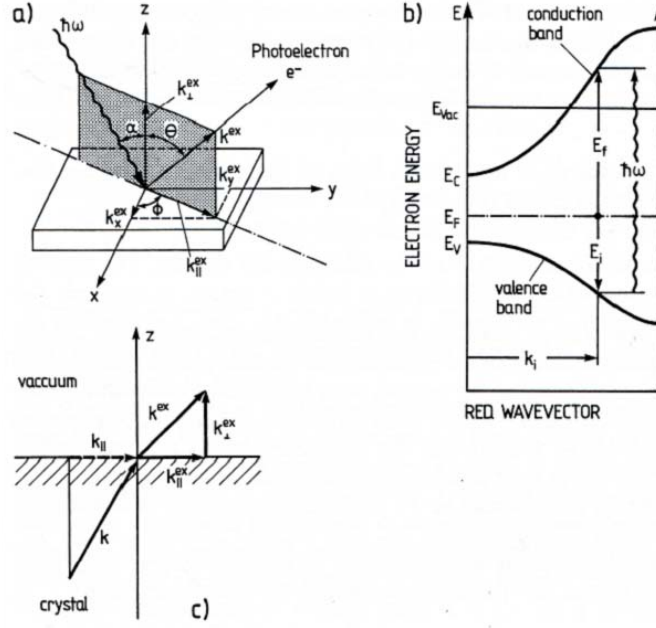


Figure 2.10: Description of a photoemission experiment. (a) Definition of the angles and wave vectors of the incident photon ($\hbar\omega$) and emitted electron e^- . (b) Representation of the photoexcitation process of a semiconductor. The energies of the initial state (E_i) and final state (E_f) are referred to the Fermi level E_F . (c) Conservation of the wave vector component k_{\parallel} (parallel to the surface) upon transmission of the emitted electron through the surface.

$$D(E, \mathbf{k}) \propto \lambda(E, \mathbf{k}) \quad (2.20)$$

Due to the fact that λ is sufficiently small to limit the probing depth, it makes photoemission a surface sensitive technique.

Step3. Escape of the electron from the solid into the vacuum.

The transmission of the electron through the surface into the vacuum requires conservation of its wave vector component parallel to the surface, as shown in Fig. 2.10(c). However, the normal component of the wave vector of photoexcited electron is not conserved during transmission process due to the broken symmetry perpendicular to the surface.

The 2D reciprocal lattice vector \mathbf{G} must satisfy the relation as described below

$$\mathbf{k}_{\parallel}^{ex} = \mathbf{k}_{\parallel} + \mathbf{G}_{\parallel} \quad (2.21)$$

In this equation $\mathbf{k}_{\parallel}^{ex}$ is measured in vacuum, i.e. outside the crystal.

The correspondence with the emission angle θ with respect to the surface normal is then given by

$$|\mathbf{k}_{\parallel}^{ex}| = \frac{\sqrt{2m}}{\hbar} \sqrt{E_{kin}} \sin \theta \quad (2.22)$$

From Fig. 2.10(b), the photoemission process shows that the relation between the initial state energy (E_i), final state energy (E_f) and the incident photon energy ($\bar{h}\omega$) must satisfy the energy conservation

$$\bar{h}\omega = E_f - E_i \quad (2.23)$$

Combining Eq. 2.11 with Eq. 2.23, with $\phi = E_{vac} - E_F$ as the work function and E_B as the (positive) binding energy referred to the Fermi level E_F , one has

$$\bar{h}\omega = E_f - E_i = E_{kin} + \phi + |E_B| \quad (2.24)$$

According to Eq. 2.21, the transmission through the surface can be described formally by the transmission rate

$$T(E, \mathbf{k}) \delta(\mathbf{k}_{\parallel} + \mathbf{G}_{\parallel} - \mathbf{k}_{\parallel}^{ex}) \quad (2.25)$$

$T(E, \mathbf{k})$ takes into account that only electrons with the positive wave vector component can be observed in the photoemission experiment.

Due to the approximation of 2D free-electron-like model, the final state bands become so closely spaced in energy to form a continuum.[28]

Considering all of the dependance and approximations during the three-step-model, the formula of the observable (external) emission current turns out to be

$$I^{ex}(E, \bar{h}\omega, \mathbf{k}_{\parallel}^{ex}) \propto \sum_{f,i,\mathbf{G}} m_{fi} f(E_i) \delta(E_f(\mathbf{k}) - E_i(\mathbf{k}) - \bar{h}\omega) \cdot D(E, \mathbf{k}) \cdot T(E, \mathbf{k}) \delta(\mathbf{k}_{\parallel} + \mathbf{G} - \mathbf{k}_{\parallel}^{ex}) \quad (2.26)$$

In real case, where the instrument resolution has to be considered, i.e. ΔE_{kin} , $\Delta\theta$ as well as $\Delta\bar{h}\omega$, the Kronecker symbols should be replaced by the relevant distribution function, for instance, Gaussian, Lorentzian, Voigt function, etc.[27]

The author will present the fitting details of the experimental data in later chapter.

2.2.4 Angle-Resolved Photoemission Spectroscopy (AR-PES)

Angle-resolved photoemission spectroscopy (AR-PES), also known as angle-resolved ultraviolet photoemission spectroscopy (AR-UPS), is a powerful technique which measures the momentum-dependent electronic band structure. Therefore, directions have to be clearly defined when performing the AR-PES measurement.

Fig. 2.11 illustrated the geometry of our experimental system, where ψ and θ is defined the incident angle and the emission angle, and normal emission is correspondent with $\theta = 0^\circ$, as shown in Fig. 2.12(a).

From Eq. 2.22, it is obvious that measuring the photoemission spectrum at different angles provides experimental energy-band structure parallel to the crystal surface.[29] Fig. 2.12 particularly exhibits that in an AR-PES measurement, the different angular dependence corresponds to the different measured ranges in surface Brillouin zone (SBZ), and it depends on the direction of the slits of the analyzer. For example, we measure along the $\bar{\Gamma}\bar{K}$ direction, i.e. $\bar{\Gamma}\bar{K}$ is parallel with the x-y plan, as shown in Fig. 2.11. In our system, the slits of the analyzer were designed in horizontal direction, so that the measurement direction in SBZ is also horizontal, as shown in Fig. 2.12(a), (b), (c). By changing θ , the electron states of different momentum are explored along $\bar{\Gamma}\bar{K}$ direction in \mathbf{k} -space and therefore the energy band dispersion along this direction is measured. The Scienta R3000 energy analyzer is specially designed so that at any emission angle θ , the spectra is 2D with energy in one axis and emission angle in another axis with spanned angle up to ± 10 degree.

2.3 Electronic States

2.3.1 Surface State

Surface is regarded as a termination of the crystal; as the result, the translational symmetry is broken in the perpendicular direction, and the periodic property of the potential has been changed. Then the surface atoms have fewer neighbors than bulk atoms, and some chemical bonds are broken at the surface. Therefore, the

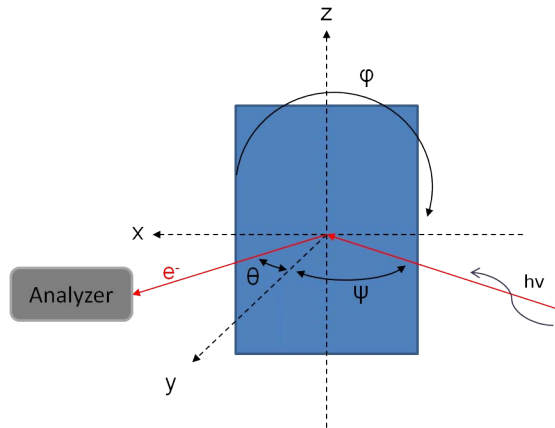


Figure 2.11: Schematically express the parameters in an angle-resolved photoemission experiment. Notice that the direction of incident light and photonexcited electrons are both in x-y plane.

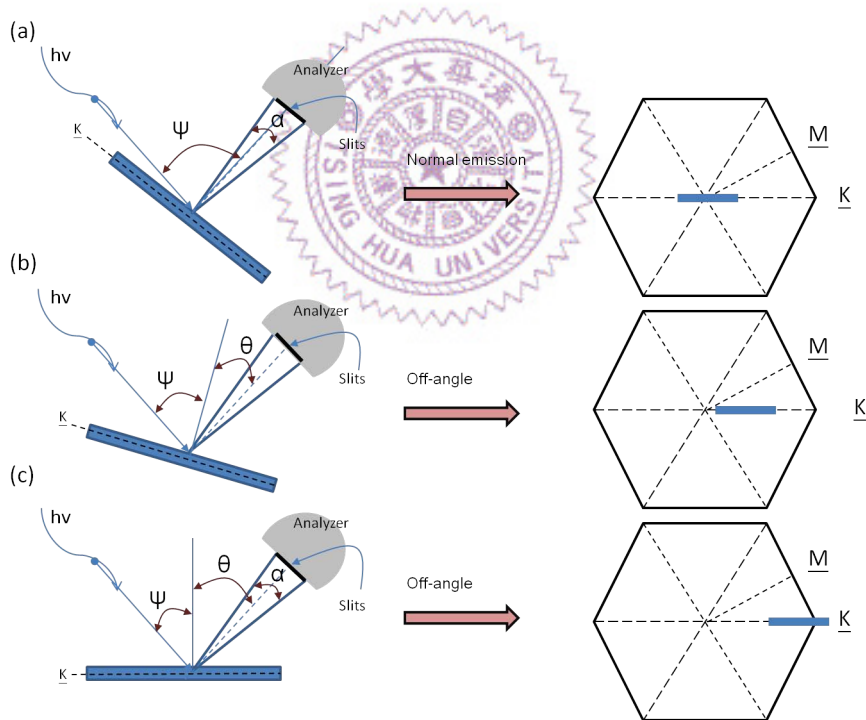


Figure 2.12: Left hand side represent the definition of relative angles between the light and the analyzer, which the slits inside are opened horizontally to the ground. Here we define the normal emission is (a), and then (b),(c) are called off-normal or off-angle. Right hand side shows the correspondence with surface Brillouin zone when we change the emission angle gradually during our measurements.

electronic structure near to the surface is markedly different in comparison with the counterpart in the bulk properties.

According to the Bloch theorem described in most of all textbook with an nearly-free-electron (NFE) model, we can solve the Schrödinger equation for an electron moving in the potential field schematically shown in Fig. 2.13(a), where a cosine variation of the potential along x direction inside the crystal is assumed. For $x < 0$,

$$V(x) = V'(e^{\frac{2\pi ix}{a}} + e^{-\frac{2\pi ix}{a}}) = 2V' \cos\left(\frac{2\pi x}{a}\right) \quad (2.27)$$

with the assumption that there is an abrupt potential step V_0 at the surface ($x=0$).

By solving this problem, we start from the regions away from the surface and allow the wave vector only real. Then we can neglect surface effects first and obtain the well-known bulk solution as described in all of the solid-state physics textbooks (Fig. 2.13(b)). In spatial regions deep inside the crystal, the form of the solution is the standing Bloch wave function ψ_{bulk} , as shown in Fig. 2.13(a). On the vacuum side, which is composed of a constant potential V_0 , the solution must be exponentially decaying due to the boundary conditions at the surface ($x=0$). Combining these solutions we can obtain a complete solution of the bulk-state wave function. There are additional solutions if complex wave vectors and considered solving the Schrödinger equation. These solutions are the surface wave functions, $\psi_{surface}$ which are essentially a standing wave between crystal surface and vacuum barrier with an exponentially decaying amplitude into the bulk, as shown in Fig. 2.13(a), and this solution also conform with the boundary conditions.

In general, the true surface-state bands are characterized by energy levels which are not degenerate with bulk bands. They can penetrate into a part of the surface Brillouin zone (SBZ). However, there are some surface derived bands degenerate with bulk states and mixing with them. These bands propagate deep into the bulk, but the amplitude of it become smaller than previous case. This kind of surface states are called *surface resonances*.

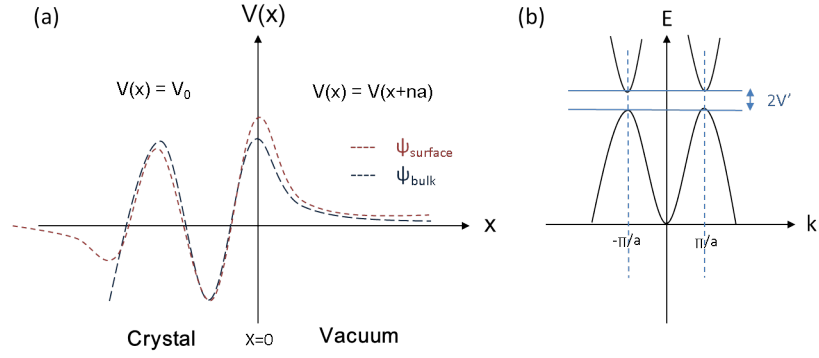


Figure 2.13: (a) Comparison between the surface wave function and bulk wave function. (b) Energy bands for one-electron bulk state.

2.3.2 Quantum Well State

Nowadays, the size of electronic devices fabricated by thin films is quite smaller than before. In light of the fundamental concept of the quantum effect, when films become thin enough and comparable with the de Broglie wavelength of the carriers (electrons or holes), quantum mechanic effects become important. In recent ten years, many researchers have done such investigations, e.g. quantum dots, corrals, wires, strips, etc.[1]

In this thesis, we focused on the confinement potential between solid-solid and solid-vacuum interface. When the films become thin enough, quantum size effect (QSE) become important. Electrons are confined between the vacuum and the film-substrate interface potential barriers. This increased localization and overlap of electronic wave functions are so called *quantum well states* (QWS). We can start from the simplest model which explained the electronic motion perpendicular to the film surface, as shown in Fig. 2.14. This crude model is just considering a free electron confined in a one-dimensional (1D) box, but it indeed serves to construct a physics image and provides some basic ideas. We can deduce the allowed wave vectors \mathbf{k}_{\perp} , energy levels $E_n(\mathbf{k}_{\perp})$, and wave functions $\psi_n(x)$ by solving the Schrödinger equation in a 1D infinite potential well, and obtain

$$\mathbf{k}_{\perp} = \frac{n\pi}{d} \quad (2.28)$$

$$E_n = \frac{\hbar^2 k_{\perp}^2}{2m} = \frac{\hbar^2}{2m} \left(\frac{n\pi}{d}\right)^2 \quad (2.29)$$

$$\psi_n(x) \propto \sin\left(\frac{n\pi x}{d}\right) \quad (2.30)$$

Generally, we can extend this results to a 2-D case and the band dispersion relation $E_n(\mathbf{k} \parallel)$ is like the free electronic dispersion. However, in actual case the potential barriers are not infinite so that the quantization condition must be modified by a phase shift which is an important quantity characterizing the boundary condition.

Fig. 2.15 exhibits the results of silver quantum well states on Ge(111). We can see each QWS peak, labeled by quantum numbers $\nu=1$ to 5, moves toward the Fermi level as the film thickness increases. This trends is because of the QSE which is governed by the Bohr-Sommerfeld quantization condition:

$$2k_{\perp} Nt + \phi = 2n\pi \quad (2.31)$$

where k_{\perp} is the wave vector component perpendicular to the film surface, N is the film thickness in monolayers, t is the monolayer thickness, and $n = N-\nu$ is a quantum number. The quantity $\phi \equiv \phi(k_{\perp}, k_{\parallel})$ is the total reflection phase shift at the two film boundaries, and it generally depends on the propagation direction of the electron wave.[3]

2.3.3 Electronic Structure of an Organic Solid

For a molecular solid, a conceptually electronic structure is schematically represented in Fig. 2.16, where the horizontal part of the potential well formed by Columbic force of the atomic nucleus is known as *vacuum level* (VL). The electrons can escape from the constraint of atoms if their energies are above the VL. Note that the experimental determination of VL is always the VL at surface, which cannot be regarded as an invariant reference level.[5][30] In addition, we can see clearly that the deep atomic orbitals (AOs) are still localized in the atomic potential well and formed

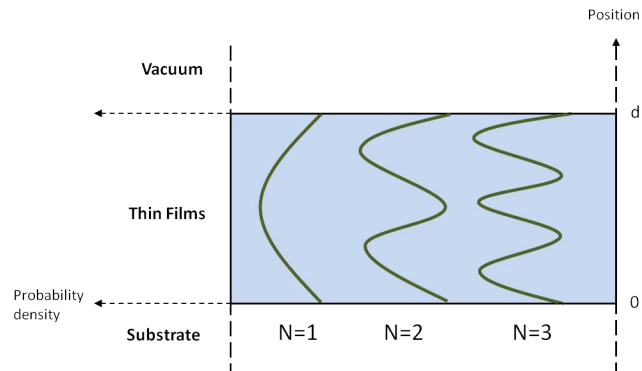


Figure 2.14: The simplest model for the quantum well effect. Within a one-dimensional box with size d , which is confined by the potentials from vacuum and substrate interface, the probability densities for the $N=1, 2$ and 3 quantum well states are schematically represented.

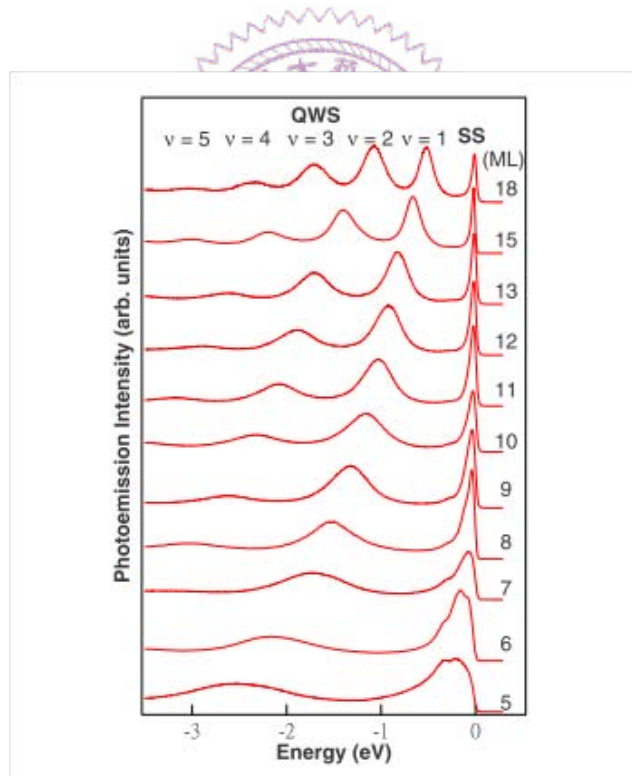


Figure 2.15: Photoemission spectra of Ag films on Ge(111) at normal emission, where $N=5$ to 18 represents the integral-layer numbers, and ν is the quantum numbers of the quantum well states.

[3]

the *core levels*. The simplified notations of the highest occupied molecular orbital and lowest unoccupied molecular orbital are HOMO and LUMO, respectively. The energy separations from the HOMO and LUMO to the VL are the gas phase ionization energy (I_g) and the electron affinity (A_g) of the molecule, respectively. Besides, the energy difference between the Fermi level (E_F) and the VL is defined as a *work function*, Φ .

In principle, a surface dipole layer may be formed right at the interface, as shown in Fig. 2.17. When the organic thin film approaches the metal substrate, a formation of the dipole layer within an electric field has been induced and slightly changed the VL position. Thus, the improvement of hole or electron injection can occur due to this effects. There are some possible reasons of the formation of the dipole layer, such as charge transfer across the interface, redistribution of electron cloud, interfacial chemical reaction, and other types of rearrangement of electronic charge. According to the energy diagram depicted in Fig. 2.17, we can obtain the relations between carrier injection barriers, Φ_B^n and Φ_B^p , and other energy levels, as described below.

$$\Phi_B^p = I_g - \Phi_M - \Delta \quad (2.32)$$

$$\Phi_B^n = \Phi_M - A_g = E_g - \Phi_B^p \quad (2.33)$$

where E_g represented the energy gap between the HOMO and the LUMO, and Δ means the shift of VL by the effect of an interfacial dipole.

As the result of an appearance of the interfacial dipole modifying the work function, we can improve both the hole and the electron injection barrier heights by depositing a few amount of organic molecules on the metal substrate. This modification is critically important for application, such as organic electroluminescent (EL) devices and spectral sensitization in photography.

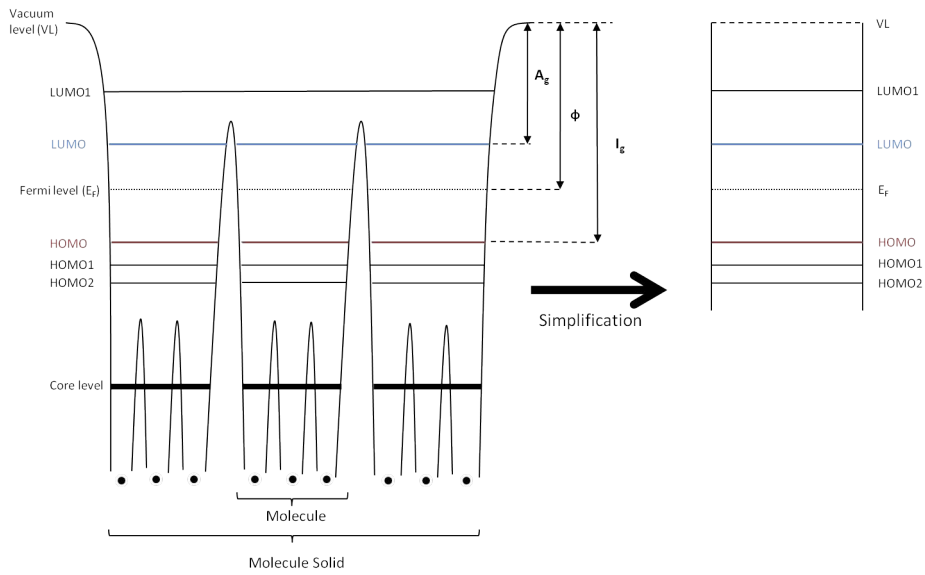


Figure 2.16: Electronic structure of an organic solid, where the vertical axis represented with potential wells, and the A_g , Φ and I_g are the electron affinity, the work function, and the ionization energy, respectively.[5]

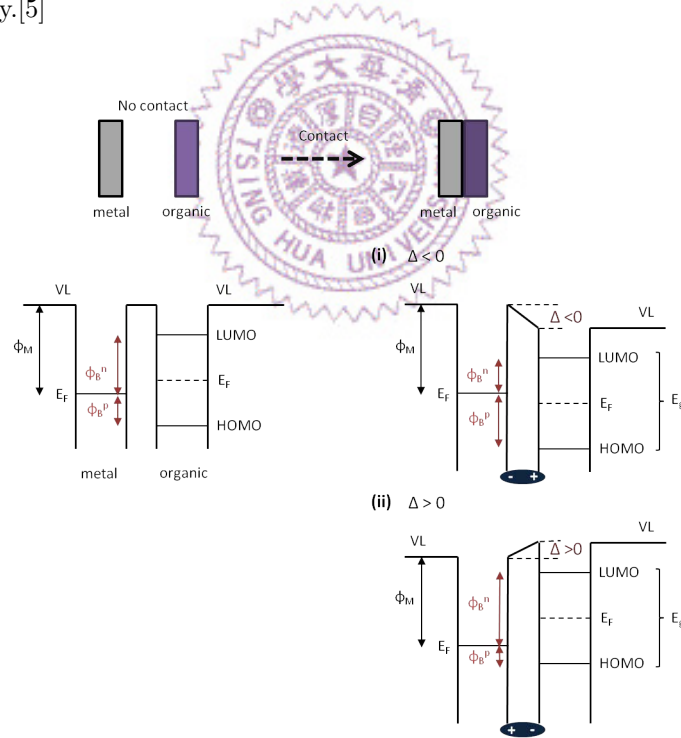


Figure 2.17: Left hand side shows an energy diagram of a metal and an organic solid separated from a relatively infinite distance. Φ_B^n and Φ_B^p denote the injection barriers for electrons and holes, and Φ_M is the work function of the metal substrate. Right hand side shows the outcome when a metal and a thin organic solid layer contact with each other. Interfacial energy diagrams of (i) a negative vacuum level shift and (ii) a positive vacuum level shift are defined.[5]

2.4 Organic Material

2.4.1 Interfacial Dipole and Energy Level Alignment

As mentioned previously, the formation of the interfacial dipole for organic/metal (also organic/organic) case indeed effects the required energy which provides the electrons for escaping from the restriction of the molecules. Numerous evidences had been particularly investigated and demonstrated in recent decade. In order to comprehend what happen to the interfacial region, researchers tend to completely realize the mechanisms of the formation of the interfacial dipole layer, which results in an energy level alignment. Nevertheless, the facts still remained unrevealed. A number of possible factors that drive the dipole formation were proposed, and then collected and classified by H. Ishii in 1999, as briefly described below.

There are four possible factors, more generally, five possibilities, including considering the intrinsic polar organic molecules, forming and affecting the interfacial dipole layer, as shown in Fig. 2.18. First, the electron transfer between the metal and the organic layer, with the positive and negative charges separated across the interface. (Fig. 2.18(a)) With regard to this point of view, the electrons transference from which side depends on how strong the acceptor (or donor) is comparing with the work function of the metal.

The second factor is the image effect or the modification of the surface dipole at metal surface. (Fig. 2.18(b)) Unlike the charge transfer effect, in this case the polarization of the electron cloud is attracted by the image charge formed in the metal, and therefore the lack of electrons at the vacuum side results in a lowering of the VL. In addition, there is an alternative explanation which also leads to a lowering of the vacuum level as described in the following. Fig. 2.18(c) display a repulsion force from the electron cloud in the adsorbate and meanwhile rearrange the electron cloud into vacuum side.

It also has possibilities that some chemical interactions occur between the organic and metal layers, as schematically show in Fig. 2.18(d). The chemical interaction

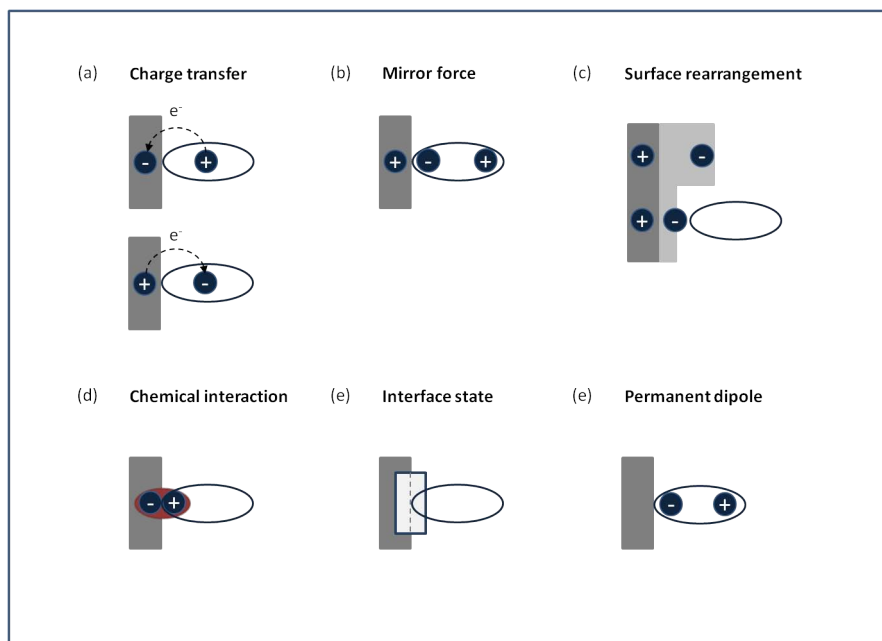


Figure 2.18: Various possibilities of the mechanisms for the interfacial dipole layer. (a) Two kinds of charge transfer across the interface. (b) Concentration of electrons in the adsorbate leading to positive charging of the vacuum side. (c) Rearrangement of electron cloud at the metal surface. (d) Strong chemical interaction between the substrate and the adsorbate. (e) Existence of the interfacial state serving as a buffer of charge carriers. (f) The polar molecules form a permanent dipole. [5]

may lead to the rearrangement of chemical bonds, or to the formation of new bonds. In this case, the direction of dipole is critically dominant. As a result, the polarity of the organic molecules could not be taken into consideration so seriously. The fourth factor is the possible existence of interfacial state, as depicted in Fig. 2.18(e). The interface state seems like a buffer at the charge exchange between the metal and the organic layers, and also will effect the value of Δ , too.

The final factor is considering the polarities for organic molecules. Institively, the orientation of the dipole moment can sufficiently provide a large interfacial dipole and result in a shift in vacuum level, as shown in Fig. 2.18(f). By using PES technique, we can precisely measure the changed behaviors of VL shift and the electronic states after depositing the organic thin films. It is helpful for us not only classifying the possible mechanisms of the formation of the interfacial dipole but the growth manners of the organic films in our system.

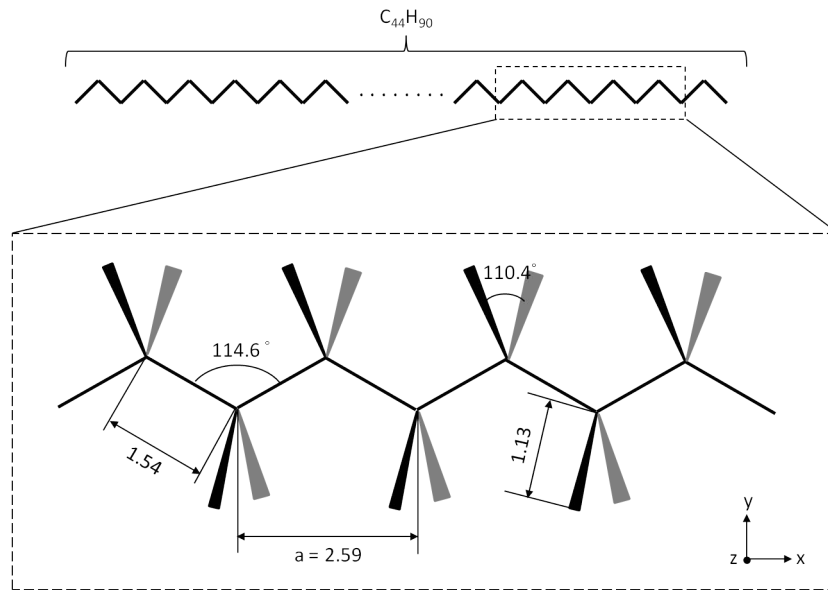


Figure 2.19: The upper illustration exhibits a tetratetracontane ($n - C_{44}H_{90}$; TTC) molecule. The coverage of dotted line enlarges only a part of the TTC molecule and the lower one shows the geometrical parameters of n-alkane, where the repeating unit length of the alkyl chain is 2.59 (Å).[31]

2.4.2 Tetratetracontane (TTC)

Tetratetracontane ($n - C_{44}H_{90}$; TTC) is a fundamental organic material, and the electronic structure has been studied well by AR-UPS for many years. We will use this section to introduce the geometrical structure, stacking orientation, and electronic properties of this well-established material.

Fig. 2.19 shows the geometrical structure of TTC, which is a material with the enormous amount of the alkyl-chain.[31] The bond lengths and bond angles of the TTC molecule are taken to be 1.54 Å (C-C bond), 1.13 Å (C-H bond), 114.6° ($\angle C - C - C$), and 110.4° ($\angle H - C - H$), respectively. Assuming the van der waals radius of hydrogen is 1.2 Å, it is easy to calculate that the chain-length and the width along the y, z direction are 57, 4.5, 4.3 Å, respectively. However, many groups had found that there are three typical orientations as schematically depicted in Fig. 2.20. We can determine which growth manner is more likely to exist in our system by means of the AR-UPS or the LEED measurement.

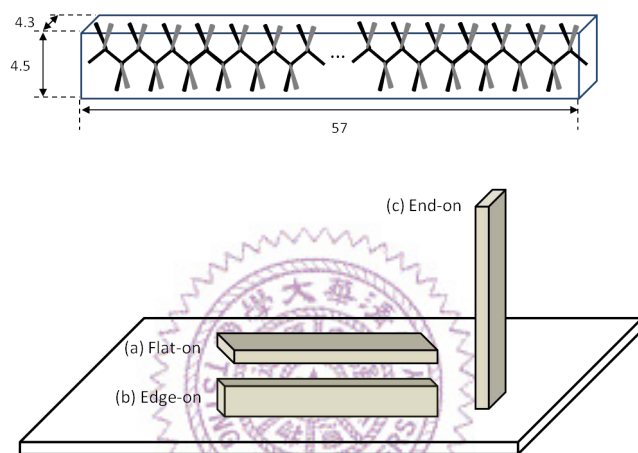


Figure 2.20: Schematically shows three typical orientation models for TTC molecule: (a) flat-on, (b) edge-on, and (c) end-on orientation. It is obvious that the C-C-C plane is parallel to the substrate surface when the orientation is flat-on; the C-C-C plane is perpendicular to the substrate surface when the orientation is edge-on, and the zigzag chain is standing on the substrate when the orientation is end-on, respectively. [31][32]

Chapter 3

Experimental Instruments and Techniques

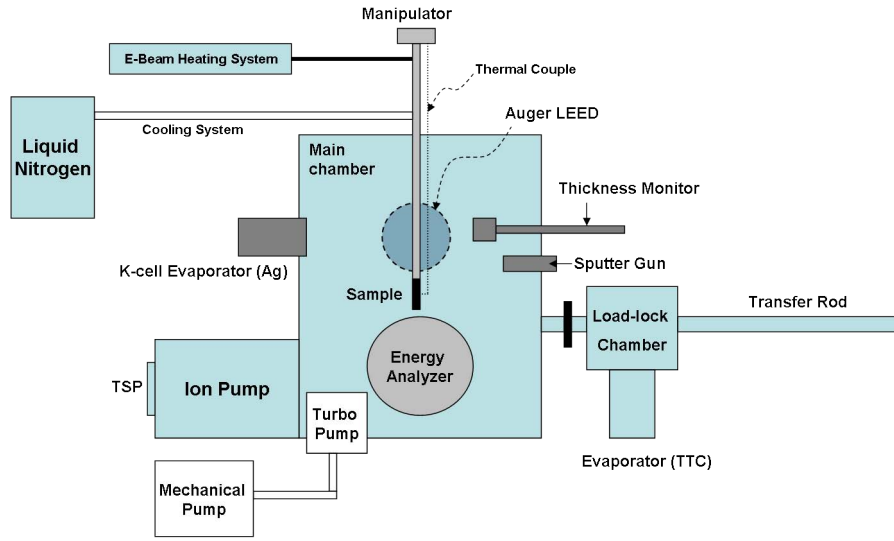
3.1 Instrumental Setup and Experimental Process

3.1.1 Instrument Setup

Fig. 3.1 schematically shows the experimental system in our laboratory, and the connections with the equipments can be mainly divided into five parts: main chamber, preparation chamber, cooling system, annealing system and pumping system (Sec. 3.2).

For the main chamber, there are the hemispherical energy analyzer (Sec. 3.3), residual gas analyzer (RGA) (Sec. 3.4), low-energy electron diffraction (LEED) (Sec. 3.5), K-cell type evaporator, thickness monitor, and a sputter gun. The manipulator is connected with a cooling system (liquid nitrogen) and a heating system (electron-beam heating), including a thermal couple. E-beam heating is that the power supply provides 5 to 1000 eV to accelerate the electrons from the filament to the sample holder, and then most of kinetic energy of electrons is converted to heat on it. The highest temperature is about 1200°C . On the other hand, by using the liquid nitrogen, the lowest temperature is about -140°C .

To avoid the contamination of the main chamber by the organic materials, we require a preparation chamber. It has an evaporator for the organic material and



S.J. Tang Photoemission Lab.

Figure 3.1: The schematic diagram of the instrumental setup in S.J. Tang photoemission laboratory.

also a pumping system, including an ion pump. The based pressure of the main and the prepared part are about 2×10^{-10} torr and 5×10^{-9} torr, respectively.

3.1.2 Sample Preparation

In this thesis, the sample was cut from a highly-doped n-type Ge(111) wafer. The sample size is about $10 \text{ mm} \times 8 \text{ mm}$, and it is welded on a sample holder by using some Tantalum (Ta) wires, as shown in Fig. 3.2.

A clean Ge(111)-c(2×8) was prepared by cycles of sputtering for ten minutes at a substrate temperature of about 500°C followed by annealing at about 600°C for ten minutes, too. For a new Ge(111) substrate, we usually need $12 \sim 16$ cycles to clean it up, and we can determine whether it is completely clean or not by LEED patterns or the photoemission spectrum of related to c-(2×8) surface structures.

From Fig. 3.3(b), it is obvious that we can observe surface state features from the energy distribution curve at normal emission if the sample is clean enough [24]; the other convenient way is by means of the sharpness of the c-(2×8) spots in LEED pattern, as shown in Fig. 3.4(a).

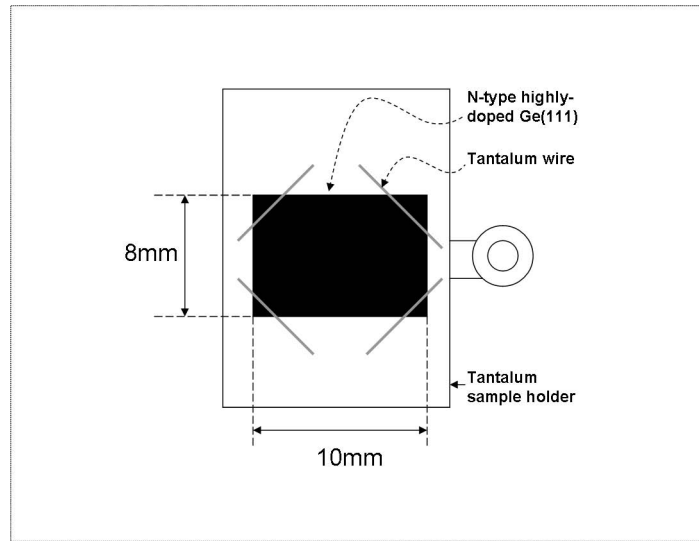


Figure 3.2: Schematic representation of the sample holder and the sample.

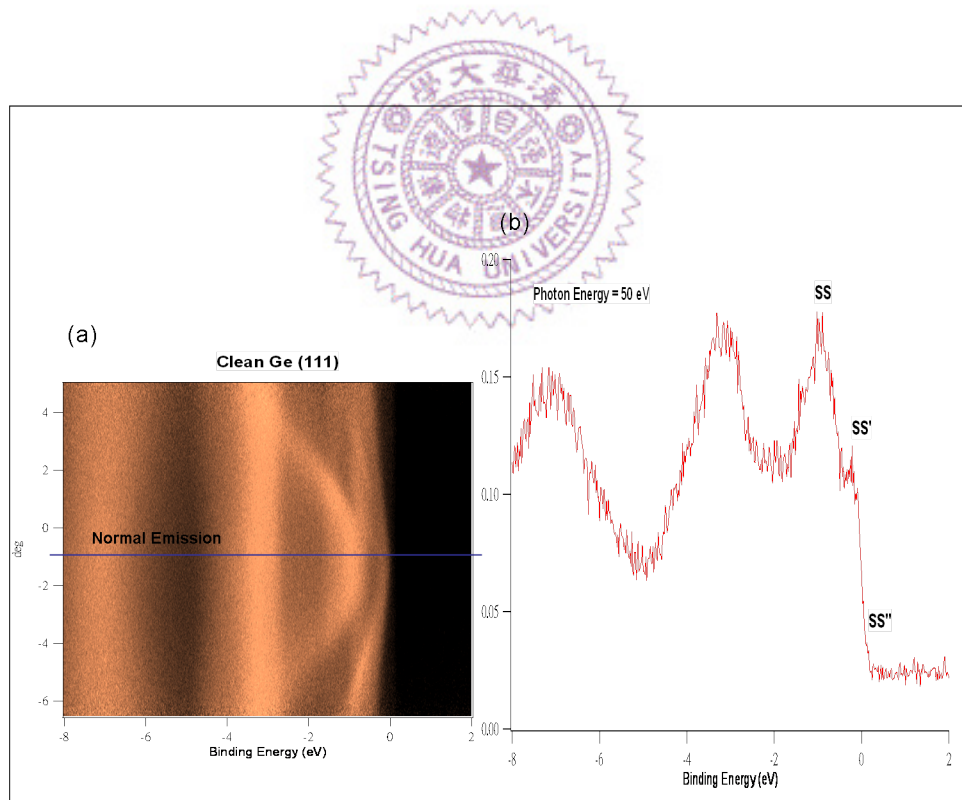


Figure 3.3: Photoemission spectrum of a clean Ge (111) substrate. (a) Angle-resolved photoemission spectrum and the applied photon energy is 50 eV. (b) The energy-distribution curve (EDC) of normal emission direction.

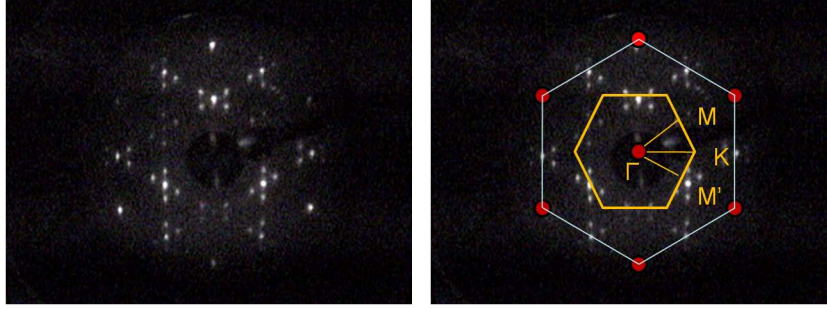


Figure 3.4: LEED pattern for a clean Ge (111) $c2\times 8$ surface, and the applied electron energy is 35 eV.



Figure 3.5: The growth model in this experiment, and the target thickness is shown on the scheme.

3.1.3 Deposition of the Silver Films and TTC Films

As shown in Fig. 3.5, we deposited the tetratetracontane (TTC) thin films on silver film in next step. After these sputtering and annealing cycles, we deposited Ag thin films on the clean Ge(111)- $c(2\times 8)$ surface. First, we needed to cool down the sample until about $-140^{\circ}C$ and then silver was carefully evaporated on it. Subsequently, the sample was annealed to $-10^{\circ}C$ and cooled back to $-140^{\circ}C$ for the photoemission measurement. Fig. 3.6 shows that the QWS intensity depend on the annealed temperature. To avoid the Ag thin film from collapsing, we should control the annealed temperature with caution. Growth at low temperature is preferable for the formation of uniform film because of reduced surface diffusion of atoms. In contrast, higher temperature usually involves larger diffusion length and kinetic effects, which are related to the interaction between diffusing atoms and atomic steps.

After the deposition of Ag thin films, we transferred the sample to the preparation chamber and evaporated the TTC at stable and low deposition rate.

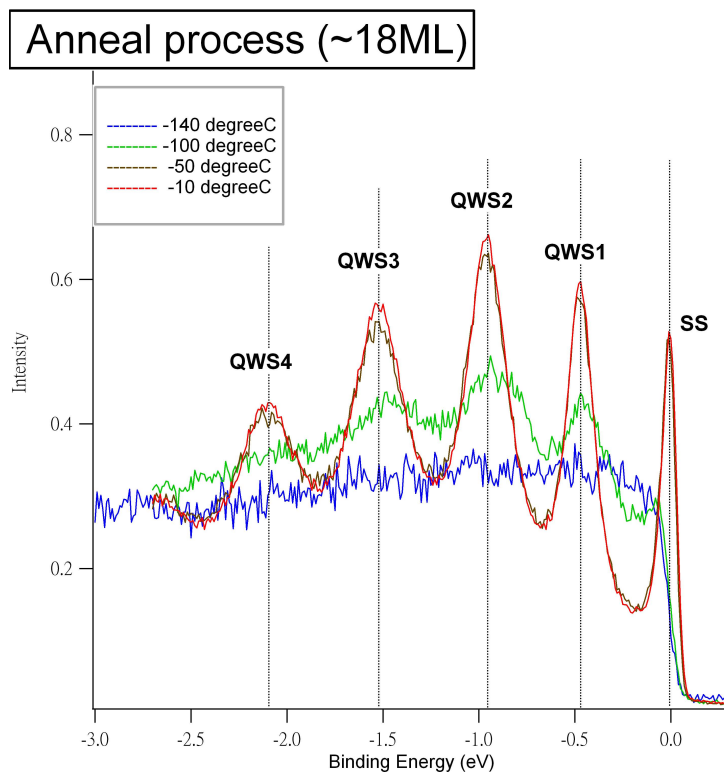


Figure 3.6: Energy distribution curve (EDC) of the different annealed temperature. Note that we measured these spectra at low temperature ($\sim -140^{\circ}C$).

3.2 Ultra-high Vacuum(UHV) Technology

3.2.1 Fundamental concept of UHV techniques

In real case, the surface of a solid exposed under atmospheric pressure is unlike an ideal system for the surface and interface physics. Accordingly, how to get a UHV condition is an important technique for surface science researches. UHV is an environment with a pressure of $10^{-9} \sim 10^{-12}$ torr (1 torr = 1.333 mbar = 133.32237 Pa·N/m²).

The particles, atoms or molecules adsorbing on it will make it hard to measure and analyze the real surface properties. Actually, it is an inevitable situation and impossible to be avoided. Thus, the quality of vacuum will determine a sample to stay clean in a long time or not. Considering this problem, an approximate *contamination rate*, R, also called the *deposition flux*, has been calculated and the result is described as [13, 18]

$$R = \frac{n\bar{v}}{4} \text{ per} \cdot \text{unit} \cdot \text{area} = \frac{p}{\sqrt{2\pi mkT}} \quad (3.1)$$

$$R\tau = N_0 \quad (3.2)$$

$$\tau = \frac{N_0}{pC} \quad (3.3)$$

where n is the molecular density, \bar{v} is the mean speed of the molecules, p is pressure of the system, τ is the monolayer arrival time, and m, k, T are the mass of an impinging gas molecular, the Boltzmann constant and the temperature of system, respectively. C can be estimated as $\frac{1}{\sqrt{2\pi mkT}}$.

Intuitively, R is linear with the pressure of environment according to the Eq. 3.1. It means that decreasing the pressure to one-half makes the vacuum twice as good.

Now, we can calculate the monolayer arrival time τ . Because CO is a major component in vacuum chamber, we will use it as an example. The molecular weight of CO is 28 and the molecular mass $m = 28 \times 1.6605 \times 10^{-27}$ kg. Assume $T = 273$ K and Boltzmann constant $k = 1.3807 \times 10^{-23}$. Substituting these value into the formula, we can find $C = 2.875 \times 10^{22} (Ns)^{-1}$.

Next, we need to find out N_0 . In this calculation we assume that there is a one to one correspondence between CO and sample surface molecules. It means that

the surface lattice constant is $a = a_0/\sqrt{2}$, where a_0 is the bulk lattice constant, and the surface mesh area is $a^2\sqrt{3}/2$. Thus, $N_0 = 9.425 \times 10^{18}$ atom/ m^2 . By the way, we also need to convert torr to SI units, namely, 1 torr = 133.32237 Pa (N/ m^2). Combining all of these factors, we get

$$\tau = \frac{1}{p} \times 2.459 \times 10^{-6} \text{ torr} \cdot \text{s}. \quad (3.4)$$

Based on this result, we can roughly estimate that at 10^{-10} torr, each surface atom is hit about once by one gas atom every 10^4 second, about once every three hours.[13]

Note that this kind of calculation missed an important factor: it is not the truth that every gas molecule which hit the sample is adsorbed on it, i.e. it is the worst situation in this calculation for a monolayer accumulation time. The amount of contaminant adsorbed on it depends on the sticking coefficients of the sample. Fortunately, most of the materials have the sticking coefficients lower than one. However, a well-defined surface with negligible contamination requires ambient pressures lower than 10^{-10} torr (10^{-10} mbar or approximately 10^{-8} Pa) so that samples remain uncontaminated for several hours.

3.2.2 UHV Instruments and Procedures

From the experimental point of view, the development of modern surface and interface physics is intimately related to the advent of Ultra-high Vacuum (UHV) techniques.[9] Basically, the typical UHV equipment consists of a stainless-steel vessel, the pumping system including several different pumps, and the pressure gauges covering different pressure ranges. The pressure range in different types of pumps are shown in Fig. 3.7.

The chamber can be made of different materials, and each material has its advantages and disadvantages. The chamber which we use is made up of μ -metal, and it is equipped with a roughing pump, a turbomolecular pump, a titanium sublimation pump (TSP) and an ion pump. μ -metal is an antimagnetic material which screened some external magnetic fields, but it is more vulnerable to high temperature so care is needed when baking.

A series of pumps must be used for the chamber to achieve a vacuum from

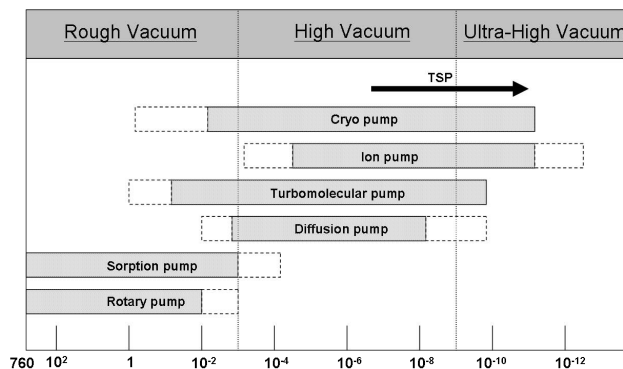


Figure 3.7: Pressure ranges in which different types of pumps can be employed.

atmosphere to UHV, and each pump has different operating pressure range. In our system, the pressure is lowered with a mechanical pump first, and the turbomolecular pump is turned on after the pressure goes down to about 10^{-3} torr. For some reasonable amount of time, the pressure will go down to about 10^{-7} torr, and we can use the residual gas analyzer (RGA) to check whether the chamber has some leakage or not. After that, the ion pump is turned on to further lower the pressure down to the order of 10^{-8} torr. Next, we need to bake the chamber next step in order to desorb mainly water molecules attached to the inner wall.

First, several heating tapes are wrapped around the chamber, and we use the aluminum foils to cover the chamber uniformly in order to distribute the heat evenly all over the chamber. The temperatures at different parts should be kept slightly different. In our system, we keep the temperature of the chamber and analyzer at about 150°C , and below 120°C , respectively. In addition, we have a load-lock system including a transfer rod and an organic evaporator. And we kept the temperature of this part about 180°C except for the evaporator. Because the evaporating point of TTC is about 180°C , we should avoid exhausting all of it during baking process. However, the temperature which we need to control around the evaporator depends on the operating condition of it.

It usually takes about 48 hours or more. After the baking process is stopped, we should immediately clean all of the filaments of the instruments inside the chamber, e.g. ion gauge, sputter gun, LEED, TSP, etc. Besides, the source and sample should be degassed, too.

The titanium sublimation pump (TSP) should be fired regularly after baking

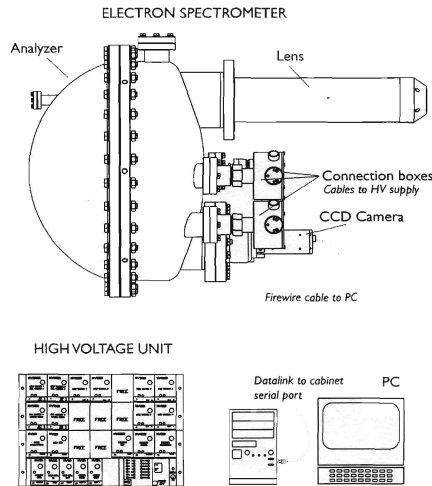


Figure 3.8: Schematic overview of the SCIENTA R3000 system parts.[14]

process has been stopped. The current which we used is 30 A for one hour first and 45 A for one hour (2 minutes/cycle). The TSP deposits a thin layer of titanium over a portion of the chamber walls, which adsorbs gas mainly hydrogen, adding to the total pumping speed.

After these process, we wait for the temperature of chamber to cool down to room temperature, and the pressure should reach about 1×10^{-10} torr or below it.

3.3 Hemispherical Energy Analyzer

3.3.1 Introduction

The hemispherical energy analyzer is the most important equipment in this system. The data in this thesis were primarily collected with the SCIENTA R3000, and it is a high-resolution electron energy analyzer developed for photoelectron spectroscopy. There are some fundamental introduction in this section. The SCIENTA R3000 consists of three main parts, which are shown in Fig. 3.8: the electron spectrometer, the supporting high voltage power supply unit and the personal computer which provides instrument control, read-out and data management.[14]

The electron spectrometer can also be divided into three major components:

- (1) Input lens for receiving charged particles
- (2) Hemispherical analyzer for spectroscopic measurements
- (3) Detector assembly with CCD camera for particle detection

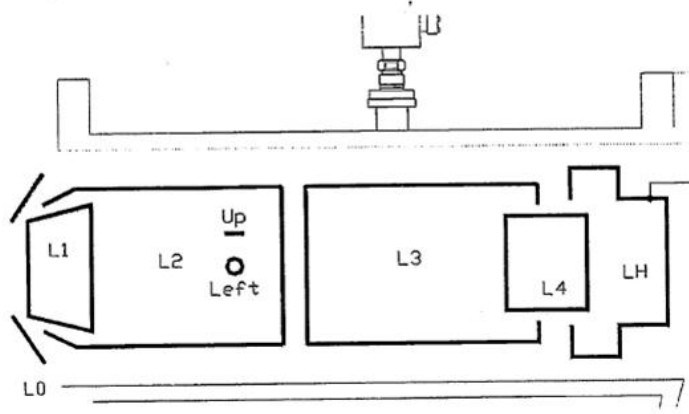


Figure 3.9: Schematic drawing of the SCIENTA R3000 multi-element lens.[14]

The analyzer with its positive charged inner sphere and negative charged outer sphere is the part of the spectrometer that performs the energy dispersion and thereby the energy measurement, and it is shown schematically in Fig. 3.10.

There is also an elaborate multi-element electrostatic lens which is shown in Fig. 3.9, collecting and transferring charged particles from a sample to the entrance slit of the hemispherical energy analyzer. The lens can be operated in two different modes, transmission and angular multiplexing imaging mode, and we will introduce it in Sec. 3.3.2. However, the fundamental theory of this hemispherical analyzer is described below.

$$E_{pass} = E_{kinetic} - eV_{retarding} \quad (3.5)$$

where $E_{kinetic}$ is the initial kinetic energy of the emission electrons and E_{pass} is the pass energy, which is a tunable parameter which affects the signal intensity and energy resolution. $V_{retarding}$ is the retarding potential provided by the electrostatic lens to slow down the electrons. The pass energy is the kinetic energy of the electron when it passes through the spherical part of the analyzer so it relies on the voltage difference between the inner and outer spheres. The relationship can be described as

$$E_{pass} = e(V_+ - V_-) \left(\frac{R_+ R_-}{R_-^2 R_+^2} \right) \quad (3.6)$$

where $R_+(R_-)$ and $V_+(V_-)$ are the radius and voltage for inner (outer) sphere.

As schematically shown in Fig. 3.10, the electron trajectories are bent in a 180° radial electrostatic field between two hemispheres with a pass energy dependent voltage difference between them. SCIENTA is equipped with six selectable slits,

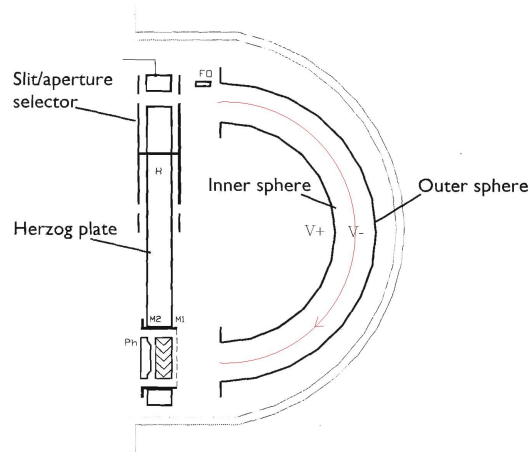


Figure 3.10: Schematic drawing of the SCIENTA R3000 analyzer.[14]

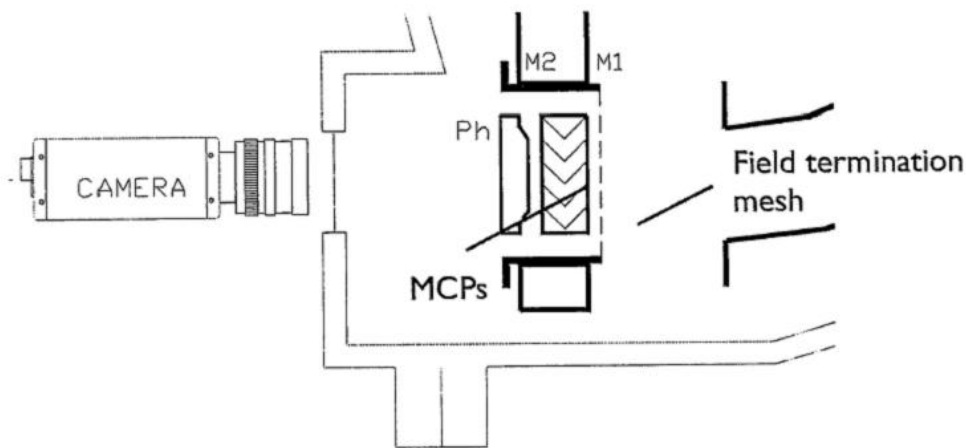


Figure 3.11: Schematic drawing of the SCIENTA R3000 detection system.[14]

three curved and three straight slits. Curved slits normally improve the energy resolution, whereas the straight slits achieve a high count rate. However, all slits have matching apertures for highest count rate at given resolution. In general, to achieve a high angular/lateral resolution in the direction perpendicular to the slit, a small slit should be used.[14]

The detection system consists of three main parts: the field termination mesh, the detector assembly (multi-channel plates (MCP) and phosphorous screen) and the FireWire CCD camera. It is a 2D detection system with energy in one direction and spatial/angular information in the another direction, so it can determine electron energies as well as the electron emission angle simultaneously. The detector area

registered by the CCD camera is squared of over 600 simultaneous energy channels and over 400 channels in the spatial or angular direction, whereas the spatial/angular dispersion is controlled by the choice of lens mode, and its schematic drawing is shown in Fig. 3.11.

3.3.2 Analyzer Modes

The energy analyzer collects photoelectrons in two dimensions as a function of energy and angle, so we can choose the different modes, transmission or angular modes, to fit our requirement during experiment.

1. Transmission Mode

Transmission mode is a standard method of lens operation. It produces an image of the sample on the detector and is intended for large-spot analysis of relatively homogeneous samples.[14] In other words, the detector measures the electrons which are emitted in a large angular range from a spot on the sample, as shown in Fig. 3.12(a). The spatial resolution in transmission mode is in the order of $300 \mu\text{m}$.

2. Angular Mode

Unlike transmission mode, angular multiplexing mode is a special way of lens operation, in which the emission angle distribution is imaged. It is used for Angle Resolved Photoemission Spectroscopy (AR-PES) measurements, which efficiently probe the band structure of solids. In this mode, the detector collects all of the electrons emitted at identical angles despite the position on the sample, as shown in Fig. 3.12(b). The angular resolution will vary with the emission spot size, where small spot size give the highest resolution.[14]

3.3.3 Energy Resolution

As mentioned above, there are two types of resolution in photoemission spectra: energy and spatial/angular resolution, but there is a trade-off between intensity (counts) and resolution. In general, the total energy resolution depends on the instruments and incident photon beam. The theoretical energy resolution of an

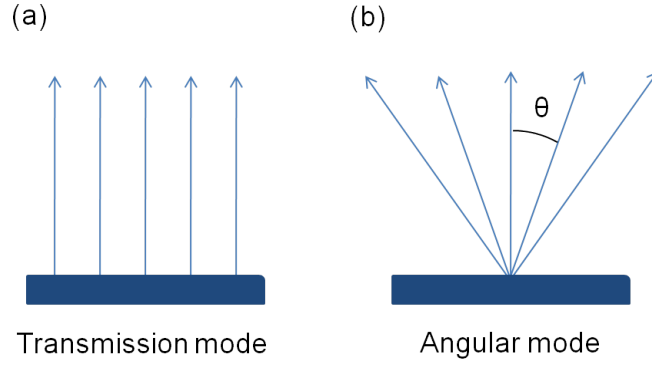


Figure 3.12: Schematically show the (a) transmission mode and (b) angular mode.

analyzer is approximated with

$$\Delta E = \frac{SE_{pass}}{2R} + f(\theta) \quad (3.7)$$

where R is the radius of analyzer, E_{pass} is the pass energy, S is the sum of the entrance and exit slit dimensions in the dispersion direction, and $f(\theta)$ is a function of the acceptance angle of the analyzer.[26] In addition, the photon beam will also affect the total energy resolution. For instance, helium lamp has a fixed resolution, and synchrotron has the adjustable slits to change the beam resolution. The total energy resolution can be expressed as $\Delta E = \sqrt{\Delta E_{analyzer}^2 + \Delta_{beam}^2}$. On the other hand, the intensity scale is approximate to $\sqrt{E_{pass}}$. We can control the angular acceptance in non-multiplexing direction, i.e. the direction perpendicular to the dispersion measurement direction, by changing the slits of analyzer.

Combining all of these dependence, the total energy resolution is described below

$$\Delta E = \sqrt{\Delta E_{photons}^2 + \Delta E_{analyzer}^2} \quad (3.8)$$

$$= \sqrt{\Delta E_{photons}^2 + \Delta E_{analyzerslits}^2 + \Delta E_{passenergy}^2} \quad (3.9)$$

We can find out the resolution, ΔE , of a system in many ways. In Fig. 3.13, the determination of Fermi level came from the line fitting between 90 percent and 10 percent of the intensity in region I and in region III, respectively, and we chose the middle part as the position of Fermi level. Here, we can also observe that the total width of Fermi edge is 109 meV, but it includes the effect of thermal broadening, $k_B T$. This spectrum was measured under room temperature, so the thermal broadening effect was about 26 meV and then we can estimate that the energy resolution

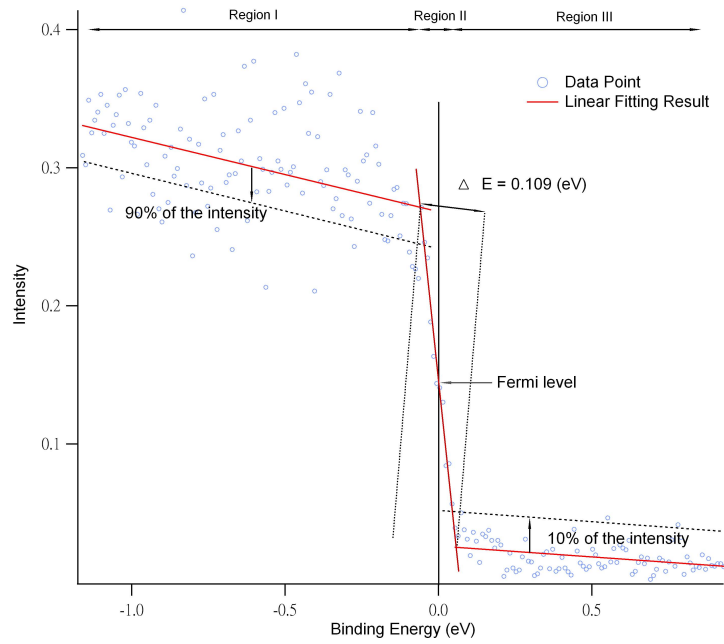


Figure 3.13:

ΔE is 83 meV.

We can also extract the energy resolution by a Fermi function convoluted with a Gaussian function, of which the full-width at half maximum (FWHM) represents the energy resolution, ΔE , of this system.

3.4 Residual Gas Analyzer (RGA)

3.4.1 Introduction

As mentioned before, achieving a ultra-high vacuum (UHV) environment is necessary for surface science. How to realize the situation inside the chamber during the experiment become a serious problem, and that is why the residual gas analyzer (RGA) is needed in this system. RGA is a mass spectrometer and also an analytical technique used for identifying the gases present in vacuum environment and, when property calibrated, can be used to determine the concentrations or absolute partial pressure of the component of a gas mixture, so it can be also called *Partial Pressure Analyzer*. We will briefly introduce the conformation, operation, and principle of RGA in later section.

3.4.2 Conformation and Principle of RGA

In our laboratory, the type of RGA which we used is SRS RGA 200, and the picture is shown in Fig. 3.14. This mass spectrometer consists of a quadrupole probe, and an electronics control unit (ECU) which mounts directly on the probe's flange, and contains all the electronics necessary to operator the instrument.[16] Besides, the total probe equipment consists of the ionizer, the quadrupole mass filter, and the ion detector.

The principle of RGA is that the molecules of gas inside the chamber are ionized by the ionizer then forming the positive ions, that is, an electron beam which is generated by a heated filament and accelerated by means of an electric field is used to strike the gas atoms. According to their different mass-to-charge ratio, these ionized molecules can be distinguished by the quadrupole mass filter which is made by four cylindrical electrodes with the two electronically opposite rods connected together, as schematically shown in Fig. 3.15.

The quadrupole mass filter is controlled by a combination of DC and RF voltages, and then the specific mass species will have stable trajectories down the quadrupole rod assembly. An entire mass spectrum is scanned by simultaneously varying the amplitude of DC and RF voltages, however, the parameters are completely calibrated at the factory so that the ECU automatically programs the RF and DC voltages on the rods to the necessary level during scans or individual mass measurements. Basically, the operation pressure is the order of 10^{-4} torr.

Upon a high-vacuum system, the primary contribution of the environment comes from hydrogen because of its light weight, and the secondary one is possible due to amount of water or carbon monoxide (CO). From Fig. 3.16(a), this RGA scan is taken before baking process, and it is obviously that the peak intensities of hydrogen [molecular weight (W_m) = 2], water (W_m = 18), carbon monoxide (W_m = 28) and nitrogen (W_m = 28) are extremely high. Fig. 3.16(b) and Fig. 3.16(c) show that the amount of water decreased during baking and after baking, respectively. Notice

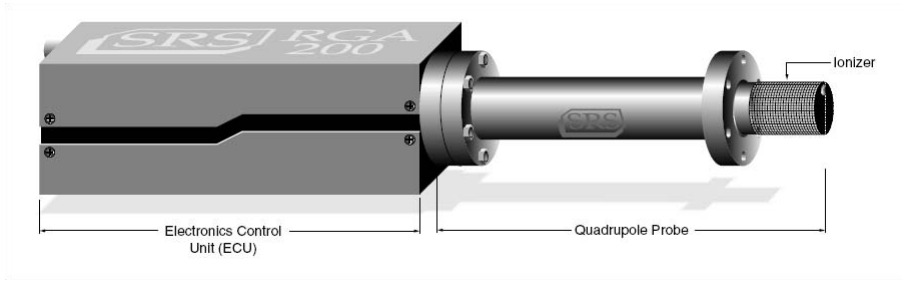


Figure 3.14: The picture of SRS residual gas analyzer.

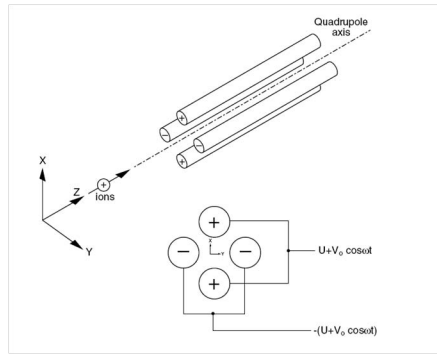


Figure 3.15: Schematic express of the quadrupole mass filter.

that the peak intensity of hydrogen is still high because of its light weight. Finally, we can find until the chamber totally cool down, as shown in Fig. 3.16(d), these components of pressure sources are greatly suppressed, and then the environment is suitable for our experiment. Here, the base pressure was often below 5×10^{-10} torr.

By the way, we also display the features when some leakages occur during achieving an ultra-high vacuum environment in Fig. 3.17. However, $W_m = 28$ is possible to be air or nitrogen. If the peak position in $W_m = 28$ is extremely higher than others, it represents there are still some leakages exist, and we shall use the RGA to check the position of leaks appeared by applying some hydrogen gas surrounding the ports in our chamber.

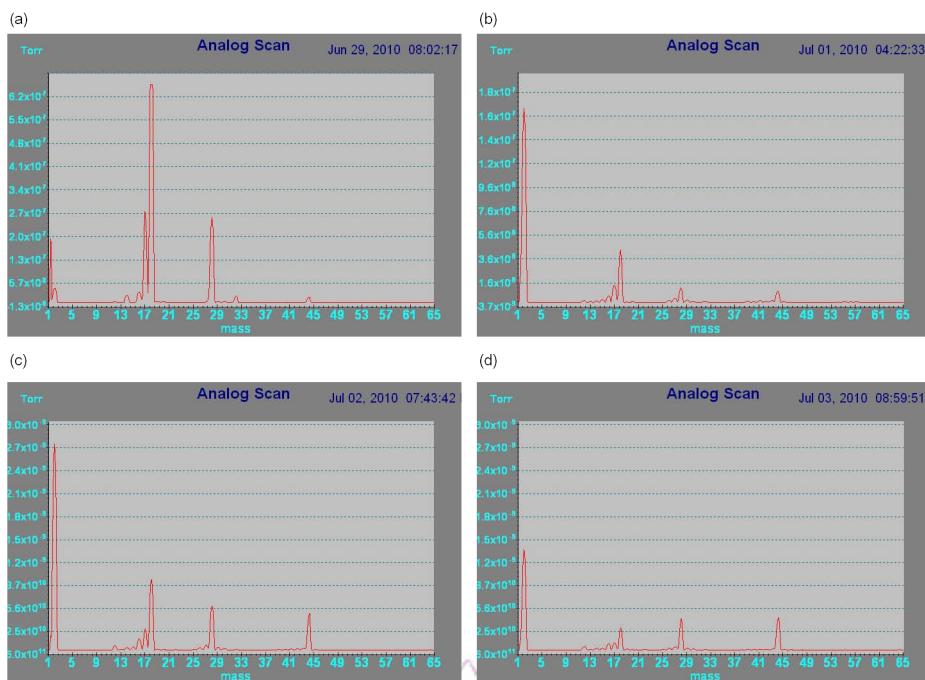


Figure 3.16: These RGA data were captured in different time, when (a) before baking, (b) during baking, (c) after baking for 10 hours, (d) after baking for 22.5 hours.

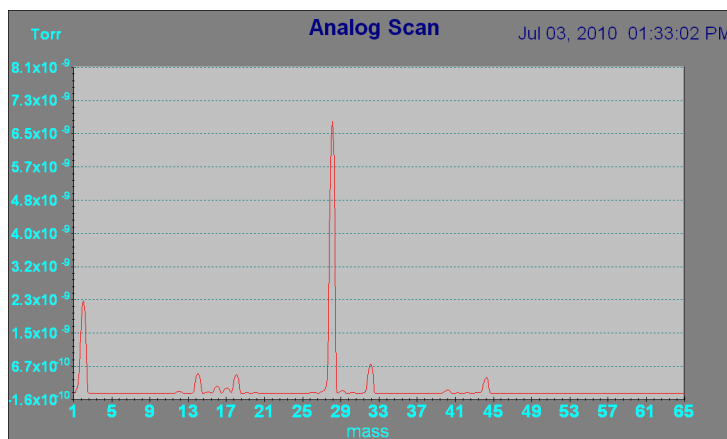


Figure 3.17: The RGA result shows when some leakages occur during an experiment. Obviously, the peak intensity of molecular weight 28 is unusually higher than others.

3.5 Low-Energy Electron Diffraction (LEED)

3.5.1 Introduction and The Kinematic Theory of Low-Energy Electron Diffraction

Low-Energy Electron Diffraction (LEED) is a principle technique for the determination of surface structures, and it is applied both to check the crystallographic quality of a freshly prepared surface or in connection with ordered adsorbate overlayers and as a means of obtaining new information about atomic surface structure.[8] The first experiment was performed almost 80 years ago by C. Davisson and L.H. Germer.[17]

According to the principle of wave-particle duality, the wavelength of the electrons given by the de Broglie relation,

$$\lambda = \frac{h}{p} = \frac{h}{\sqrt{2mE}} \quad (3.10)$$

where h is Planck's constant. We can easily estimate that when electron kinetic energy (E) is 20 eV, the de Broglie wavelength of electrons is approximate 2.738 Å. This value corresponds to an atomic dimension, i.e. LEED is quite a proper technique in surface science since the range of wavelength of electrons employed is seen to be comparable with atomic spacings. This fortunate coincidence forms the basis for LEED from solid surface.

In principle, the two-dimensional Laue conditions for an elastic Bragg diffraction electron are satisfied,

$$\mathbf{K} \cdot \mathbf{a} = 2\pi h, \mathbf{K} \cdot \mathbf{b} = 2\pi k \quad (3.11)$$

With $\mathbf{K} = \mathbf{K}_{\parallel} + K_{\perp}\hat{e}_{\perp}$, Eq. 3.11 is fulfilled when

$$\mathbf{K}_{\parallel} = \mathbf{k}'_{\parallel} - \mathbf{k}_{\parallel} = \mathbf{G}_{\parallel} \quad (3.12)$$

where \mathbf{K} is the scattering wave vector; h, k are integer, and \mathbf{a}, \mathbf{b} are the basis vectors of 2D unit mesh within the surface. \mathbf{k}_{\parallel} and \mathbf{k}'_{\parallel} are the scattering vector component parallel to the surface before and after scattering, respectively.[17] Note that this condition is valid for the limiting case where only the topmost atomic layer is involved in scattering.

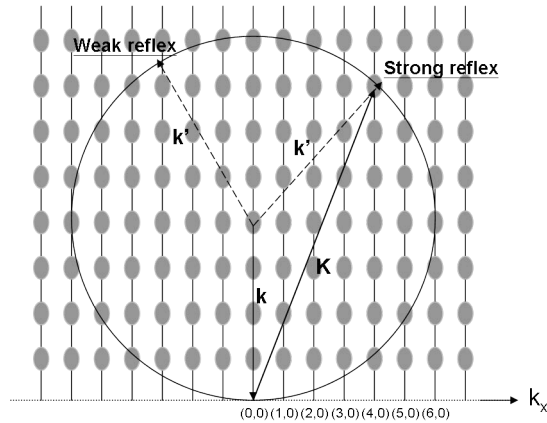


Figure 3.18: Ewald construction for elastic scattering on a quasi-2D surface lattice. The "thicker" regions of the rods arise from the third Laue condition, which cannot be completely neglected.

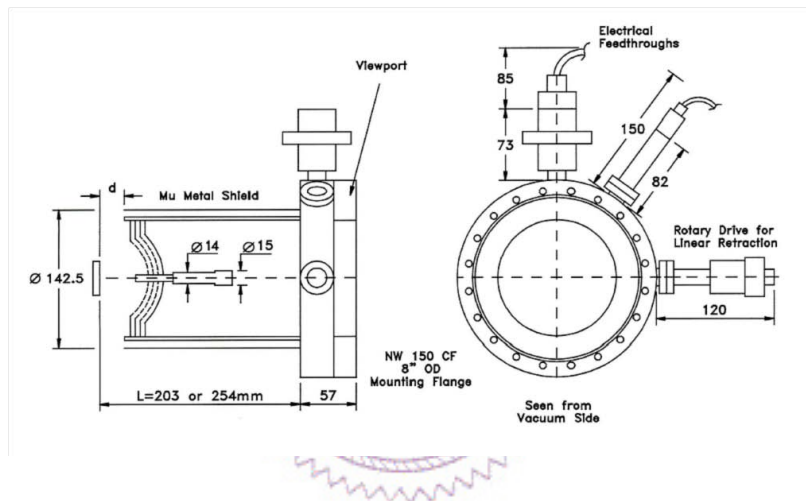


Figure 3.19: Schematic drawing of the SPECTRALEED.[15]

In LEED experiment, the primary electrons penetrate into the solid for several atomic layers. The deeper they penetrate, the more scattering events in the z-direction perpendicular to the surface contribute to the LEED pattern.[8] It leads to a modulation of the intensities of the Bragg reflections in comparison with the case of pure 2D scattering. Fig. 3.18 shows Ewald construction for elastic scattering on a quasi-2D surface lattice. The "thicker" regions of the rods arise from the third Laue condition, which cannot be completely neglected.

3.5.2 Conformation and Operation of LEED

In our laboratory, the instrument we used for LEED measurement is OMICRON SPECTRALEED of which, the diagram is schematically shown in Fig. 3.19. From

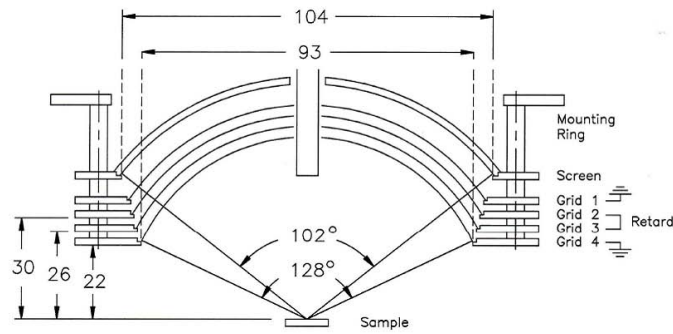


Figure 3.20: Geometrical dimensions of the SPECTRALEED Optics. Grid 1 is grounded via the power supply, and Grid 3,4 are grounded inside the optics. Grid 2 is the only retard grid.[15]

the left hand side in Fig. 3.19 or Fig. 3.20, we can see that there are four grids and an electron gun inside it; meanwhile, shows the geometrical dimensions of it. In general, electrons emitted from a heated filament of the electron gun are accelerated by an electrostatic lens with apertures and incident normally on the sample. The sample itself must be a well-ordered surface structure in order to generate a back-scattered electron diffraction pattern. There is a fluorescent screen (collector), which has to be positively biased in order to achieve a final acceleration of the slow electrons.

Elastic scattering electrons respond with the high-energy electrons and which can be visible on the screen. On the contrary, inelastic scattering also occurs at the sample surface, thus giving rise to the electrons of lower energy and producing a relatively homogeneous background illumination of the phosphor screen. In order to reduce these inelastic scattering electrons, the middle grid is applied a somewhat negative bias, as shown in Fig. 3.20.[8] However, the defects or crystallographic imperfections will also increase the background and broaden the size of spots.

Because of the vertically incident angle, the diffraction maxima can be directly associated with the reciprocal lattice and the LEED pattern represents the symmetry of the surface. We will show some results in a latter chapter.

In our experiment, we applied 1.15 A for the filament current and -27 V for the Wehnelt basically. And we always capture the LEED patterns by using CCD camera in the dark surrounding to prevent the light from reducing the quality of our pictures.

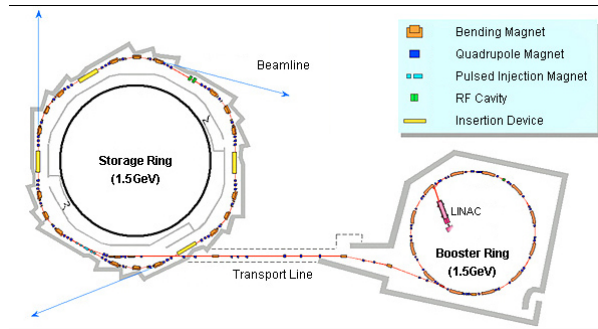


Figure 3.21: The accelerator systems at NSRRC comprise a 1.5-GeV injector and a 1.5-GeV storage ring. The injector consists of a 50-MeV linear accelerator(LINAC) and a 1.5-GeV booster synchrotron.[21]

3.6 Synchrotron Light Source

3.6.1 Introduction of Synchrotron Radiation

Originally, high-energy physics used synchrotron accelerators to investigate elementary particles at the beginning of 20th century. In 1947, synchrotron radiation was "accidentally" discovered in an electron synchrotron of General Electric Company, USA by J. Schwinger.[20]

The fundamental theory of synchrotron radiation is very simple. According to electromagnetic (EM) mechanic, if the electrons are centripetally accelerated, they will emit the light. It is just a common concept in EM field, but it indeed brings about some extremely changes in science research and development. Afterwards, scientists gradually realized that there are many useful characteristics of synchrotron light, and specialized accelerators were developed as dedicated light sources. These are the second-generation synchrotron radiation source.

In Taiwan, the Taiwan Light Source (TLS) had begun operation in 1993, which is the first committed third-generation synchrotron radiation source in Asia. The difference between the second and the third one is the specially-designed magnets, called wigglers and undulators, which were inserted in storage rings to deflect the electron beam many times over a short distance. Comparing with the previous generation synchrotron, this optimized design enlarged the photon fluxes over one

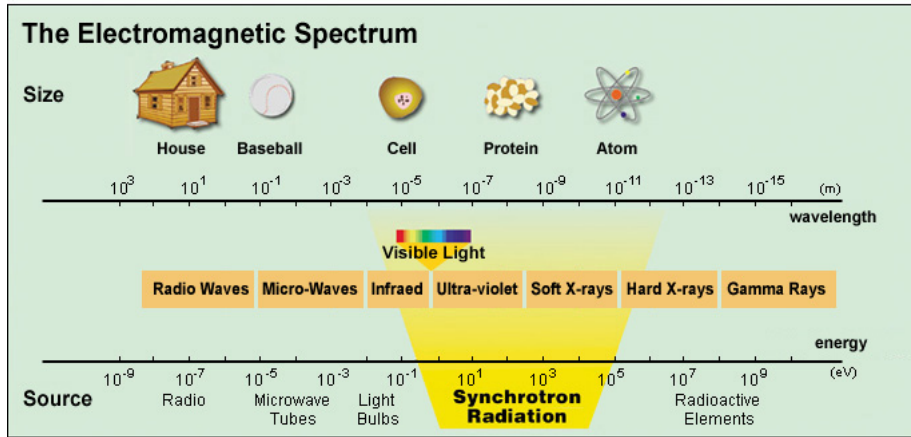


Figure 3.22: [21]

thousand times through the accumulation of emitted synchrotron light. The synchrotron radiation has many advantageous properties, e.g. high intensity, continuous spectrum, excellent collimation, low emittance, pulse-time structure, polarization, etc.[21]

In National Synchrotron Radiation Research Center (NSRRC), the synchrotron radiation refers to a continuous band of electromagnetic spectrum including infrared, visible light, ultraviolet, and X-rays., as shown in Fig. 3.22. The lights of different wavelengths are used for different purposes.

3.6.2 Beam-line Specifications

All of the photoemission data in this thesis were collected at a 6m low-energy spherical grating monochromator(6m-LSGM) beamline(BL-08A) in NSRRC, Taiwan.

This is a beamline which covers the photon energies from 20 to 200 eV. Fig. 3.23 shows the calculated fluxes as a function of the photon energies for three different gratings. We can choose the proper grating to satisfy our requirements of experiment. The LSGM beamline achieves the maximum photon throughput and energy resolving power by using the spherical optical elements and a movable exit slit. It consists of one horizontal focusing mirror (HFM), one vertical focusing mir-

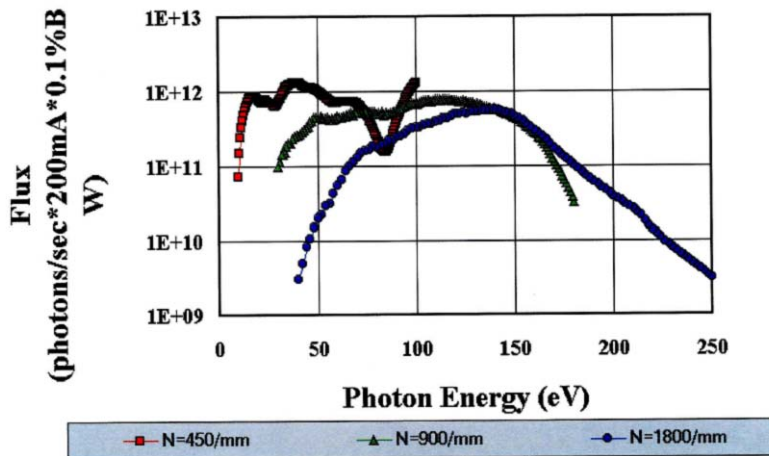


Figure 3.23: [21]

ror (VFM), one spherical grating monochromator with 3 gratings, and one toroidal refocusing mirror (RFM). The front-station is connected with the vacuum chambers of storage ring, and consists of several valves, monitors and one radiation-shielding block. Our chamber is connected to the beamline as the end-station and the primary photon energy which we used in this experiment is 50 eV, because the QWS of Ag films has best cross-section at 50 eV. Thus, the grating which we used is 450/mm to obtain the best photon fluxes for this photon energy.

Chapter 4

Well-ordered Ultrathin Film of Tetratetracontane (n-C₄₄H₉₀; TTC)/Ag thin film/Ge(111)

4.1 Electronic Structure and Molecular Orientation

Because we must gradually deposit the organic thin films on Ag thin films and also decrease the radiative damage, we did not do the LEED measurement during our experiment this time. Therefore we only did AR-UPS measurement and speculate the molecular orientation of TTC on Ag thin films by the UPS spectra. The results are elucidated in this chapter, including the band dispersion of the HOMO peak, the vacuum level shift, and the changes of the Ag QWS, etc.

Fig. 4.1(ii) shows the energy distribution curves (EDC) at $\theta = 0^\circ$ before and after the deposition of TTC thin film. Notice that the surface state disappeared when we deposited a monolayer TTC film on Ag films, and Fig. 4.1(iii) shows the corresponding 2D AR-PES. The observed quantum-well-state (QWS) bands outside the band gap of Ge are known as quantum-well-resonance (QWR), which has partial transmission and partial reflection at the interface, as indicated by the green arrow. The 4d band structure of the Ag substrate is also observed in the binding-energy region of about 4 to 8 eV.

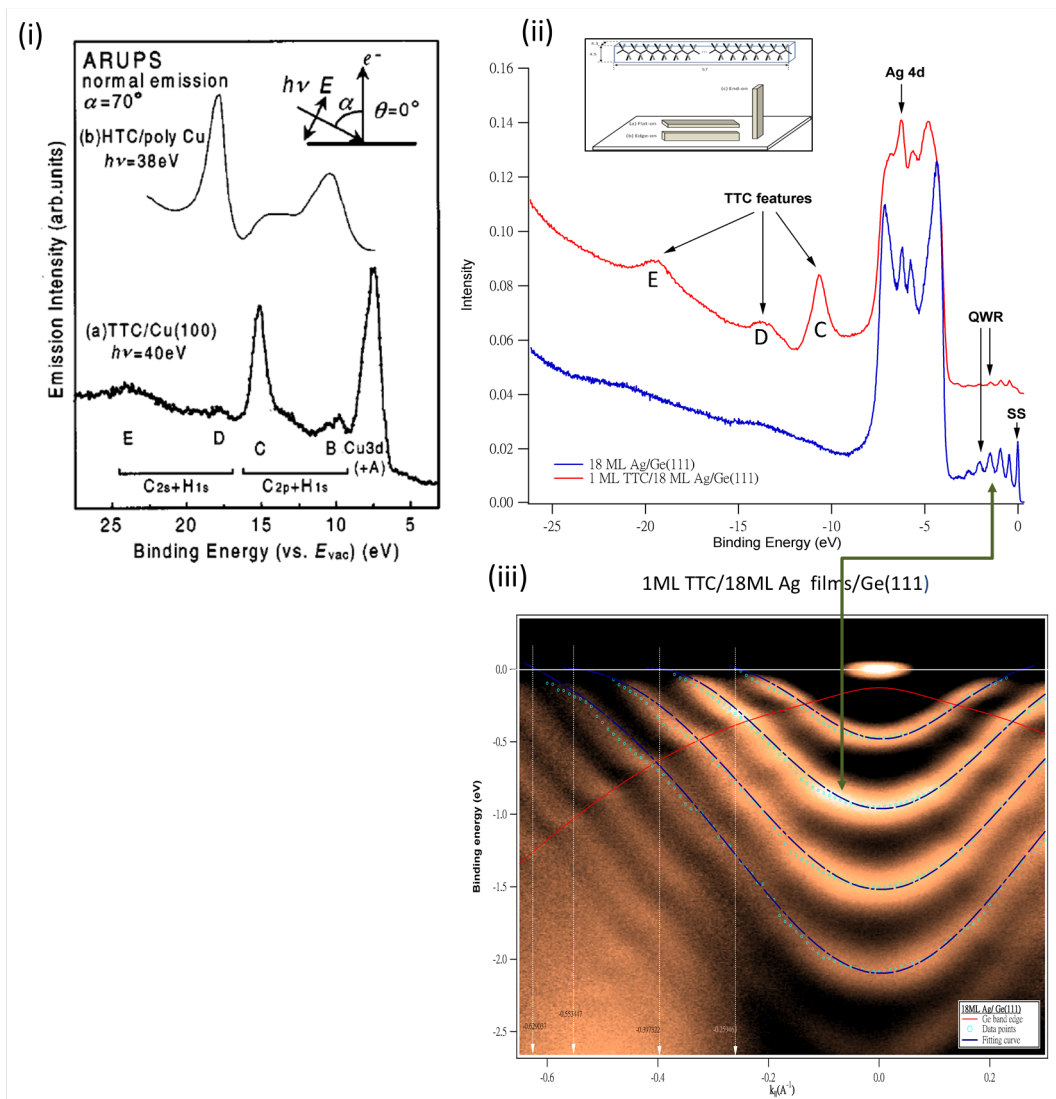


Figure 4.1: (i,a) Normal emission spectrum of a TTC thin film on Cu(100). The incident photon energy is 40 eV. (i,b) Normal emission spectrum of an end-on-orientated HTC film on contaminated Cu polycrystalline plate. (ii) EDCs of a wider binding-energy spectrum, where the blue and red curves are 18 ML Ag/Ge(111) and 1 ML TTC/18 ML Ag/Ge(111), respectively. (iii) The 2D AR-PES for 1ML TTC/18ML Ag thin films/Ge(111).

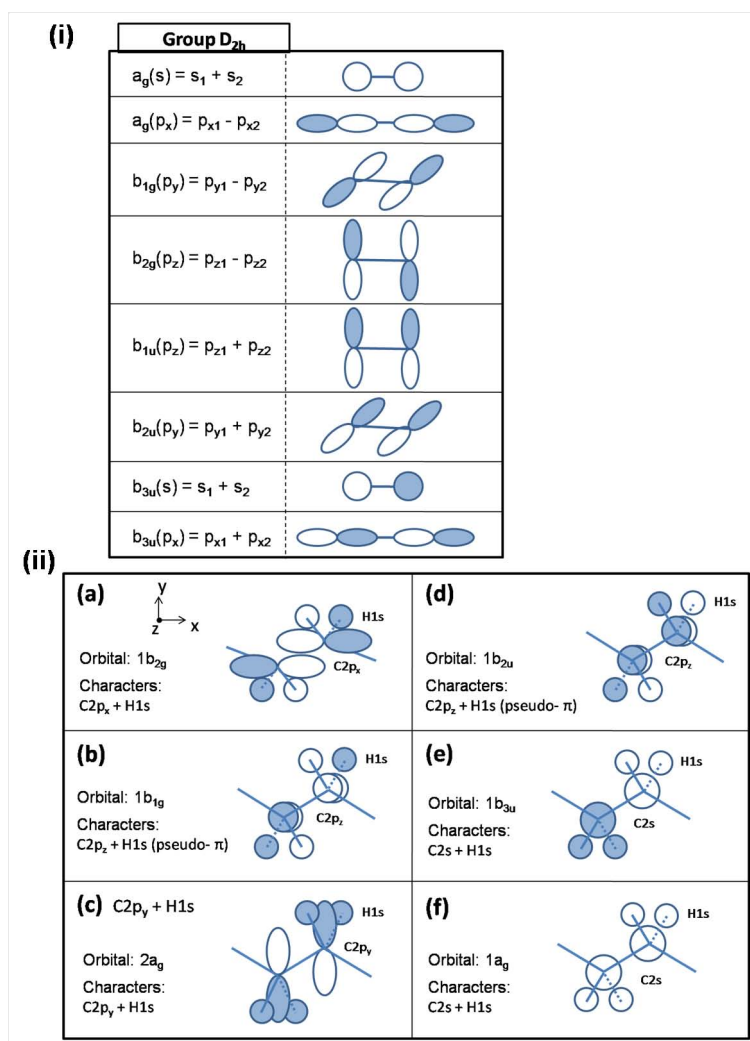


Figure 4.2: (i) The functional forms of the factor group D_{2h} . [33] (ii) Schematic representation of molecular orbitals for polyethylene. [31]

According to the previous reports, which was published by D. Yoshimura in 1999, the normal emission spectrum of TTC thin film/Cu(100) and HTC film on contaminated Cu polycrystalline plate are shown in Fig. 4.1(i). The observed binding energies of the electronic states for TTC/Cu(100) are 5.3 (peak B), 10.6 (peak C), 13.4 (peak D), 19.5 (peak E) eV, which are relative to Fermi level. The peak B and the peak C are derived from the $C2p_y+H1s$ bands and the $C2p_z+H1s$ bands, respectively. The peaks D and E are derived from $C2s+H1s$ bands.[31, 32] The symmetry elements for free all-trans polyethylene at the Γ point is isomorphous with the factor group D_{2h} , as shown in Fig. 4.2(i).[33] The corresponding molecular states are schematically shown in Fig. 4.2(ii). For TTC thin films/18 ML Ag films/Ge(111) shown in Fig.4.1(ii), the observed binding energies of the electronic states at $\theta = 0^\circ$ are 10.64 (peak C), 13.68 (peak D), and 19.53 (peak E) eV, which are consistent with the results of TTC/Cu(100).

As mentioned in Sec. 2.4.2, there are three possibilities of molecular orientation, flat-on, edge-on and end-on orientations. Due to the fact that the spectrum of the end-on molecules is drastically different from our result,[36] which is shown in Fig. 4.1(i,b). We can exclude this possibility from our case. According to the report, the peak C and peak E can be allowed only for the flat-on and the edge-on orientation, respectively. The peak D can be allowed for both the flat-on and edge-on orientations. Since the intensities of peak C and peak E are relatively stronger than the peak D, we conclude that the molecules on top are almost the flat-on orientation and few of disordered film.

4.2 Band Dispersion

Fig. 4.3 shows the 2D AR-PES for 1 ML TTC/18 ML Ag/Ge(111) at the binding energy ranging from 0 to 26 eV. Fig. 4.4 show the comparison of the angle-dependence spectra between (a) TTC/Ag thin film/Ge(111) and (b) TTC/Cu(100). The value of θ varies from 0° with step 2.5° .

Comparing with TTC/Cu(100), we had good agreements with them and also

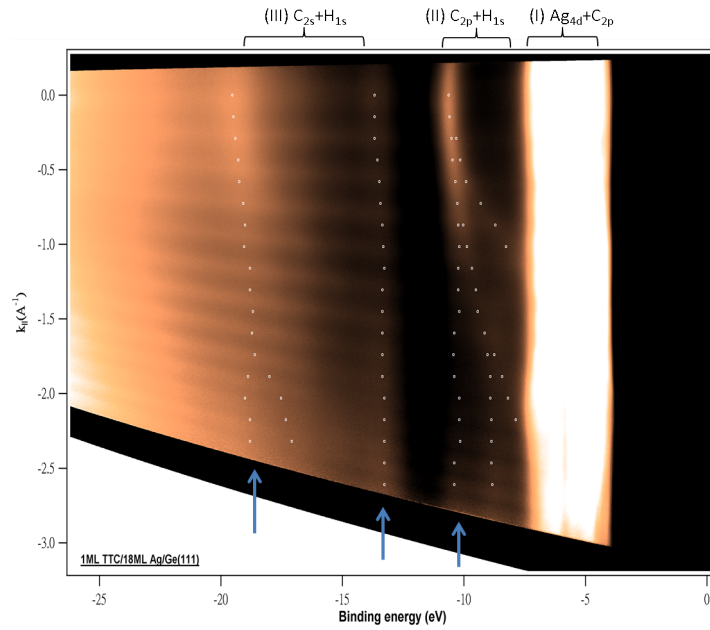


Figure 4.3: The 2D ARPES for 1 ML TTC/ 18 ML Ag/ Ge(111). Several TTC features were observed in this region.

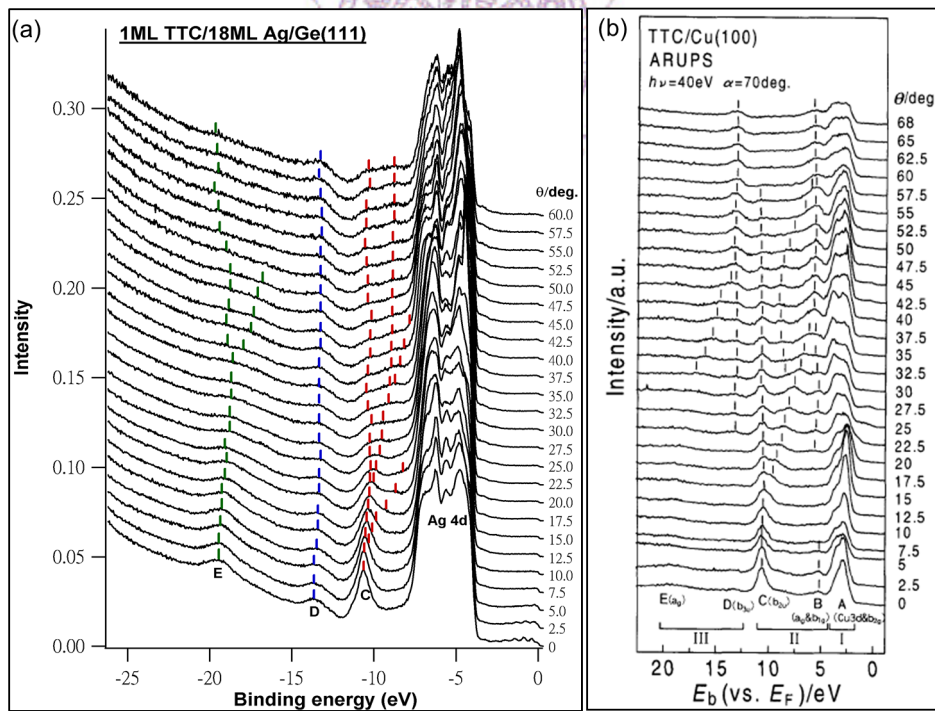


Figure 4.4: The dependence of the AR-UPS spectrum on the take-off angle (θ) for (a) 1 ML TTC/18 ML Ag film/Ge(111) and (b) 1 ML TTC/Cu(100). The abscissa is the binding energy relative to the Fermi level (E_F), and the value of θ varied from 0° with step 2.5° .

some discrepancies.[32] We compared the energy-band structures between two cases, 1ML TTC/18ML Ag film/Ge(111) and 1ML TTC/Cu(100), as shown in Fig. 4.5. It is plotted in a reduced zone scheme, where the red circles represent the data points in 1st BZ. The lengths of repeating units of alkyl chain a is 2.59 Å, and leads to the width of the BZ boundary ($k_{\parallel} = \frac{\pi}{a}$) of 1.21 Å⁻¹. Due to the fact that Ag(111) is in hexagonal shape, the TTC molecules arrange to an included angle 60 degree. The width of the BZ boundary ($k_{\parallel} = \frac{\pi}{\sqrt{3}a}$) is 0.7 Å⁻¹.

As observed, there are some discrepancies between two cases in the reduced zone scheme. We attribute this to the TTC molecules aligning 60 degrees with the others, due to the three-fold symmetry of the substrate. In Fig. 4.3, structure I is due to Ag 4d orbital and upper edge of C2p derived orbital of TTC. Structure II and III are due to C2p+H1s and C2s+H1s orbitals, respectively.[32] According to the report, there are two TTC molecular states (symmetry at Γ) with binding energy ranging between 2 to 6 eV hidden by the Ag 4d peak.[31]

As shown in Fig. 4.3 and Fig. 4.5, the blue arrows indicate the inter-molecular dispersion with the alkyl-chain axes vertical to the plane, $\phi = 90^\circ$ (see Fig. 2.11), in which the wave-vector component along the alkyl chain is always zero. So that, these flat dispersions are observed in both cases. Notice that the band dispersions are decreased comparing with TTC/Cu(100). From the surface zone center to surface zone boundary, the energy change of the band is 4.5 eV for TTC/Cu(100) but 2.4 eV for TTC/Ag thin films/Ge((111)). Unlike the two-fold symmetry in TTC/Cu(100), the observed inter-molecular bands disperse along $\phi = 0^\circ$ and $\phi = 90^\circ$. Due to the three-fold symmetry in this system, we observed the dispersions along $\phi = 60^\circ$, and this fact results in decreased band dispersion comparing with TTC/Cu(100).

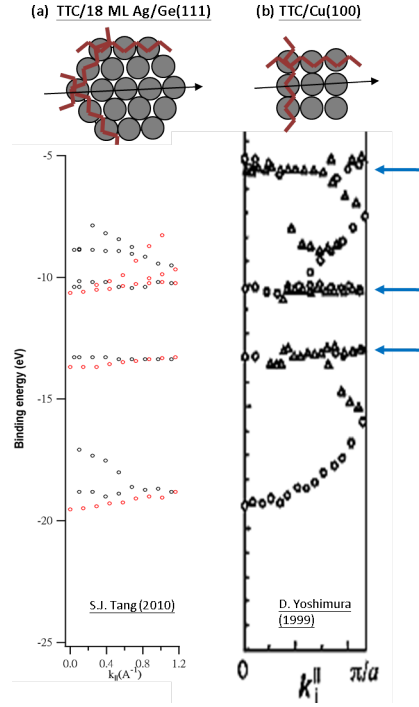


Figure 4.5: Experimentally obtained energy-band structure plotted in the reduced zone scheme for (a) TTC/18 ML Ag/Ge(111) and (b) TTC/Cu(100).

4.3 QWS Change

4.3.1 Analytic Methods

Fig. 4.6 shows the fitting processes for the 2D angle-resolved photoemission spectrum. Each 2D spectra is composed of 600 slices, corresponding to energy distribution curves (EDCs) or momentum dispersion curves (MDCs). I then fitted the EDC and MDC by the lorentzian functions and Fermi function with a polynomial background, as shown in Fig. 4.6(b). From the fitting we can extract the positions of QWS to map out their energy band dispersions, as indicated by red circles in Fig. 4.7. They were the fitted with the model

$$\varepsilon(k_{\parallel}) = \varepsilon(0) + \frac{\hbar^2 k_{\parallel}^2}{2m^*} \frac{1 + a k_{\parallel}^2}{1 + b k_{\parallel}^2}, \quad (4.1)$$

in which the ratio of polynomials is a Padé function employed to account for the band distortion; a, b, and the zone center effective mass m^* are treated as fitting parameters. Fig. 4.7 shows the fitting result of 2D angle-resolved photoemission spectrum for 18 ML Ag on Ge(111), where the red circles represent the peak positions

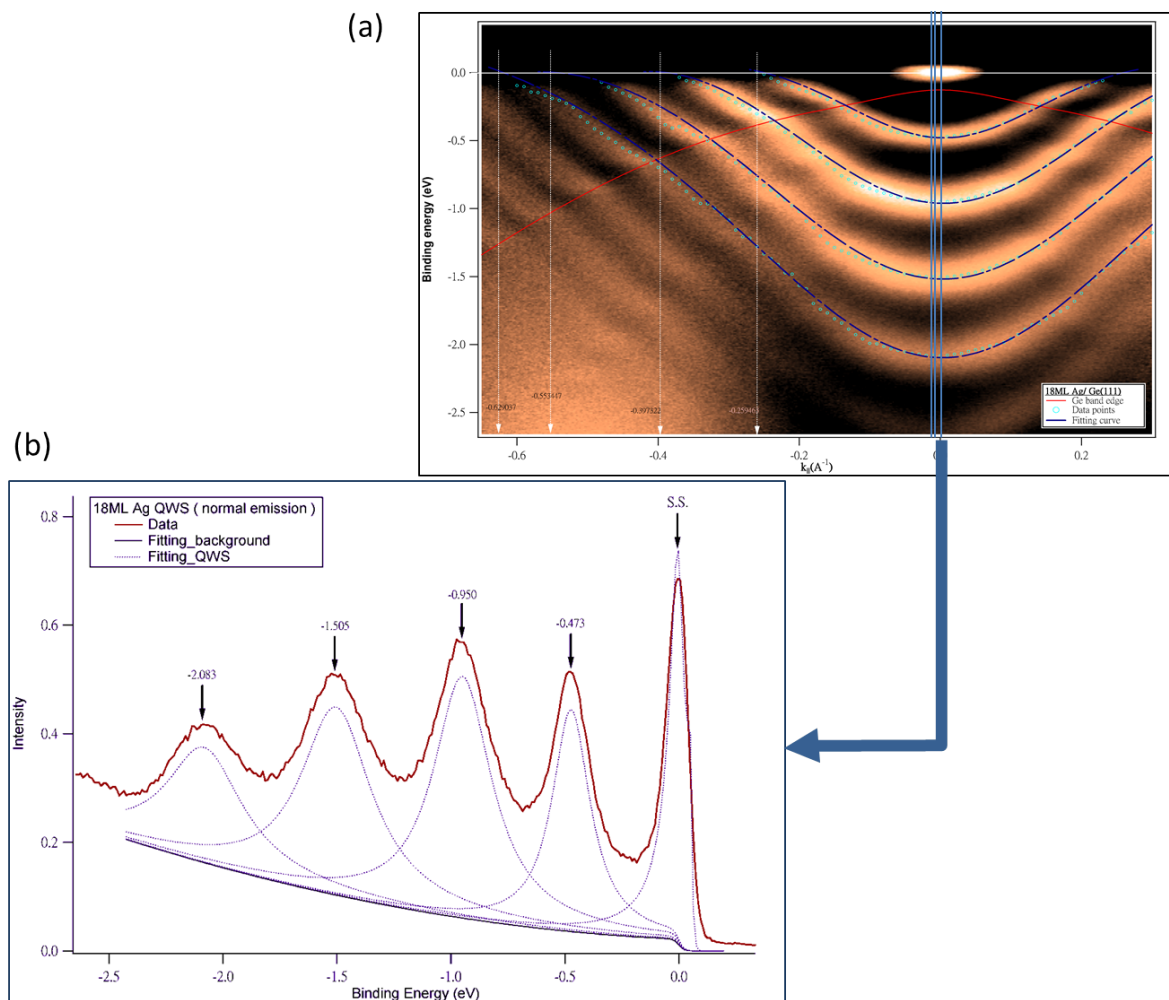


Figure 4.6: The fitting processes for the 2D angle-resolved photoemission spectrum. (a) Angle-resolved photoemission spectra for 18 ML Ag on Ge(111) in the symmetry direction from $\bar{\Gamma}$ to \bar{K} . The EDC is extracted between every ten slices and pointed out the peak position by curve fitting. (b) An EDC at photoelectron emission angle $\theta = 0$. Purple dash line and blue one are fitted by the second degree background and the Lorentzian profile, respectively.

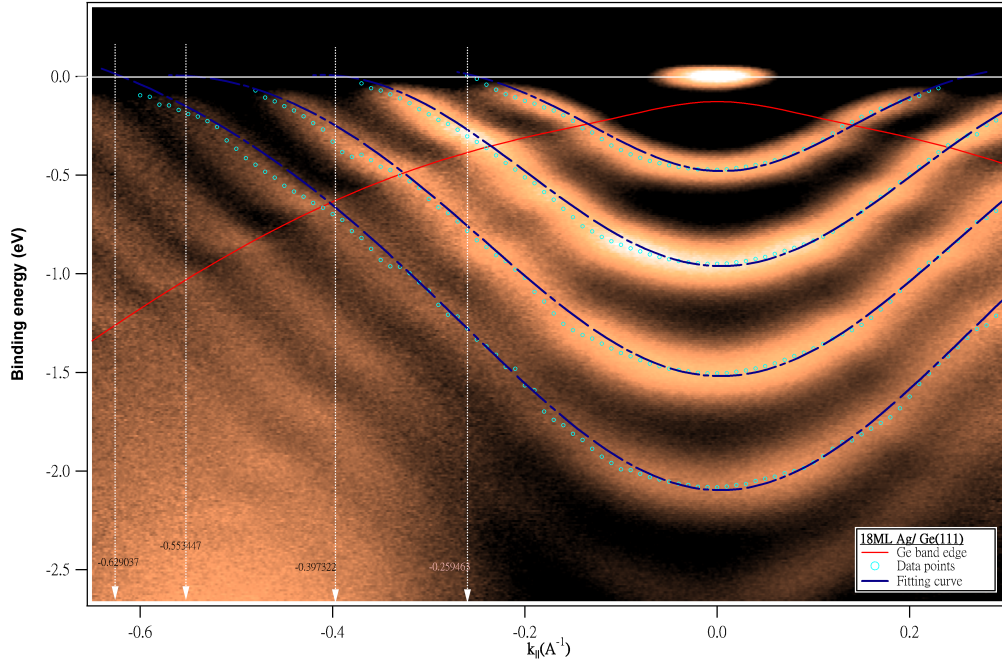


Figure 4.7: The 2D angle-resolved photoemission spectrum for 18 ML Ag on Ge(111). The data points (red circles) are the peak positions of the fitting results, and they are then further fitted with the model as described in Eq. 4.1.

in different EDC or MDC, and the blue lines are the fitting results from Eq. 4.1.

4.3.2 Results and Discussions

We observed that both the intensities and energy positions of Ag QWS change after we deposited TTC thin film on 18 ML Ag films. Fig. 4.8 shows that QWS first shift towards Fermi level when the thickness of TTC reaches 1 ML, and then away from Fermi level. That implies the Fermi surface enclosed by the QWS bands shrinks and the occupied charge should decrease at 1ML. Here we discuss the behaviors more particularly in the system of 1 ML TTC/ 18 ML Ag/ Ge(111).

As seen from Fig. 4.9, the QWS dispersions as a function of in-plane momentum (k_{\parallel}) relative to the normal emission are parabolic with positive curvatures, indicating free electron nature. The effective mass of each QWS band can be extracted from the fitting model of Eq. 4.1. Table 4.1 shows the fitting results of effective mass before and after depositing 1 ML TTC on the Ag thin film. Notice that the values of the effective mass did not change evidently, so we speculated that the QWS bands

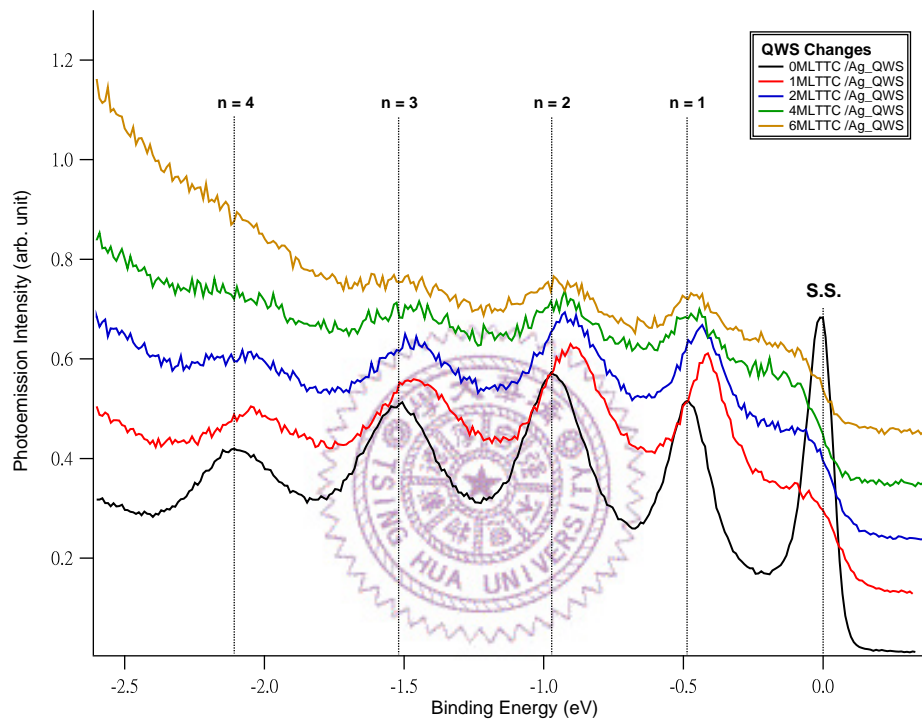


Figure 4.8: EDC for TTC films at various coverages. These curves are extracted from normal emission, i.e. $\theta = 0$. Note that the surface state (S.S.) (black curve) was extremely sensitive to TTC molecules. The red curve shows a maximum shift of the binding energies for the quantum well states. The shift is about 0.08 eV towards the Fermi level.

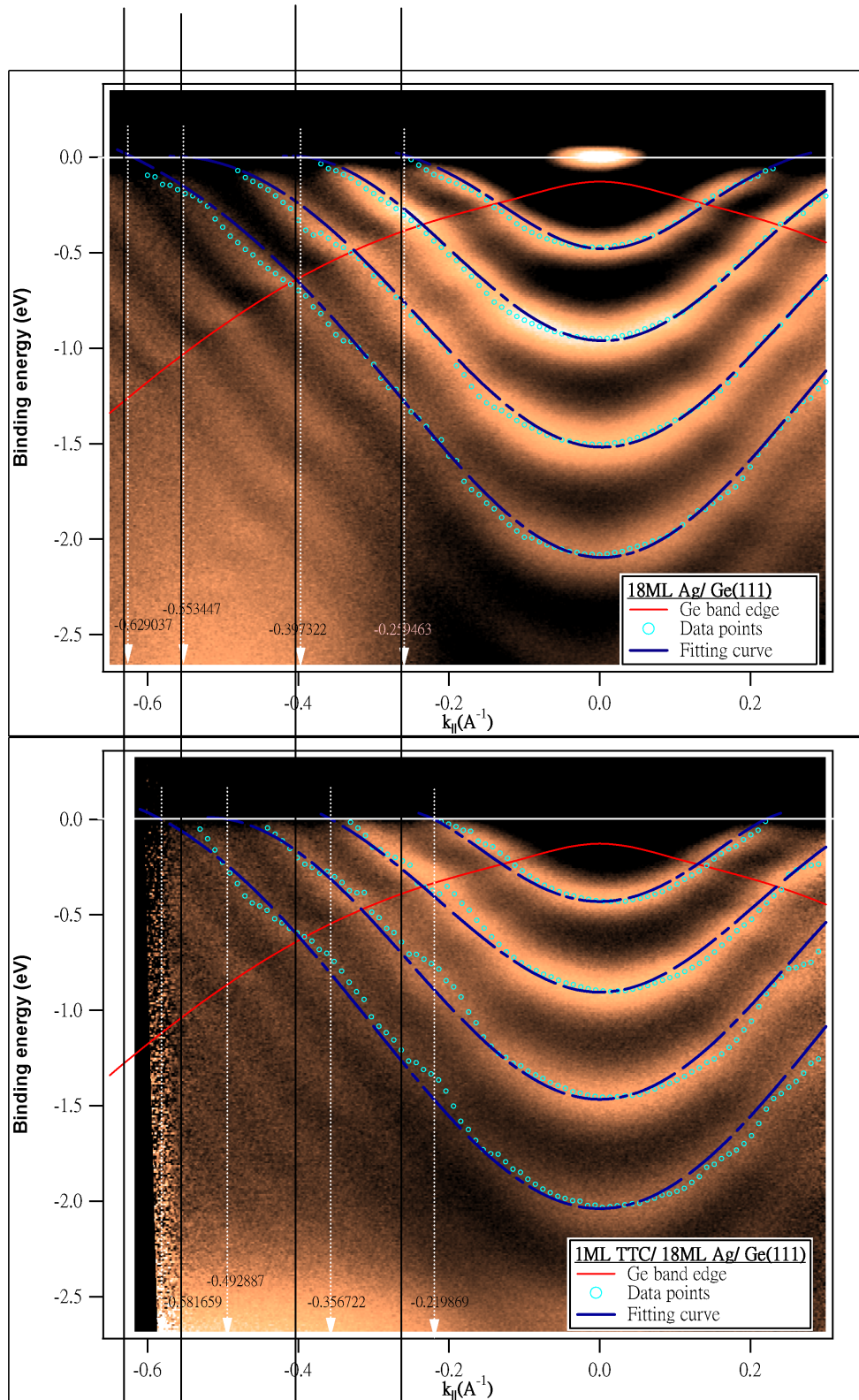


Figure 4.9: The variations of the 2D AR-PES for Ag valence bands before and after TTC deposition. The Ag QWS shifted slightly toward the Fermi level and changed the Fermi wave vectors, so that the occupations of QWS should be decreased. Notice that the surface state (S.S.) was sensitive to the TTC molecules and disappeared with 1 ML TTC on top.

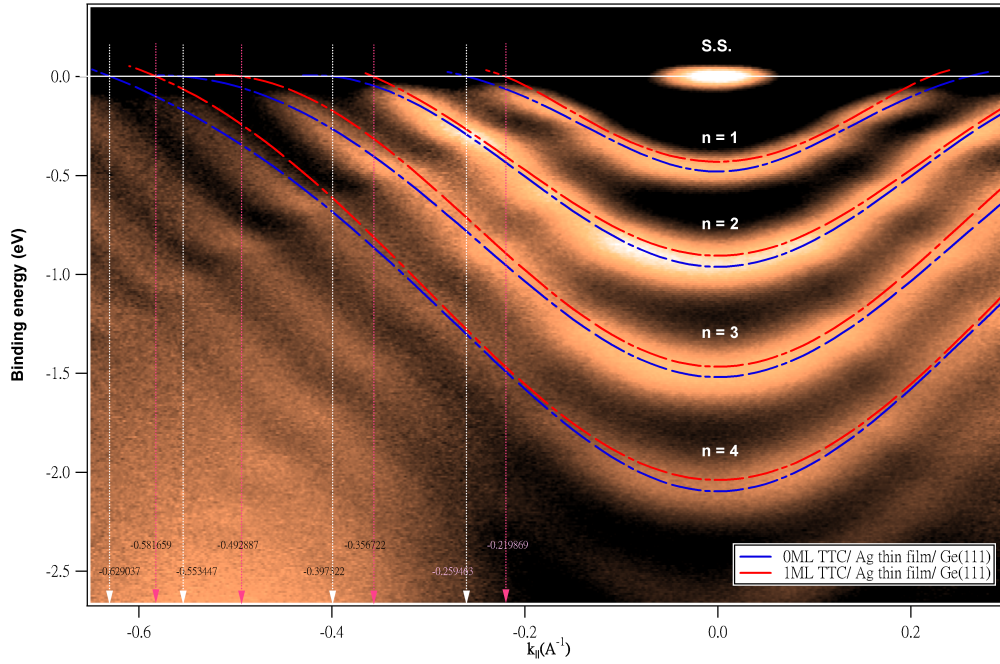


Figure 4.10: The combination of the fitting curves for Ag QWS, where the crosses were the data points, and the red and blue curves were the fitting results of QWS with and without 1 ML TTC thin film, respectively.

shifted in energies simply due to the charge effect and the Fermi surface enclosed by each QWS retains its shape after the deposition of TTC thin film.

We calculated the decreased populations of QWS through the change of Fermi surface area. We assumed that the Fermi surface is roughly a circular form and the area of the whole surface Brillouin zone (SBZ) corresponds to two electrons per surface silver atom (spin up and spin down). For QWS with different quantum number $n = 1$ to 4, the corresponding decrease in charge density is 0.0225, 0.0364, 0.0757, 0.0687 electrons per surface silver atom, respectively. From Sec. 2.4.2, we can deduce that the TTC surface density is 0.0565 TTC molecules per surface silver atom. This would correspond to 0.3991, 0.6443, 1.3407, 1.2158 electrons per TTC molecule for each QWS described above.

As shown in Fig. 4.8, the adsorption of 1 ML TTC on 18 ML Ag on Ge(111) leads to about 0.08 eV shift of binding energy of the QWS. This small shift of QWS indicates that the metallic electronic states are not strongly affected by the presence

		m^*/m_e			
Thickness \ QWS	N = 1	N = 2	N = 3	N = 4	
0 ML	0.25074	0.26646	0.26950	0.24456	
1ML	0.28163	0.27091	0.28218	0.29432	

Table 4.1: The values of effective masses before and after deposition TTC molecules with each QWS.

of the TTC layer. On the other hand, the surface state would be affected a lot by the TTC molecules since its amplitude has large percentage of distribution outside the surface of the thin film. Fig. 4.9(a) and Fig. 4.9(b) clearly indicate the Ag surface state is completely destroyed after TTC being deposited while QWS shifts in energy due to the special charge effect at the interface.

4.4 Vacuum Level Shift

4.4.1 Experiment and Analytic Methods

In our system, we applied a bias with -6 V between the sample and the analyzer in order to ensure that the onset of these second-order-electron spectra could appear on the region of "plus" kinetic energy, and also, make sure the cutoff is not determined by the work function of the energy analyzer.[31] The incident photon energy is 50 eV. Fig. 4.11(a) shows a non-normalized cutoff spectrum for one monolayer (ML) TTC/ 18ML Ag QWS on Ge (111) by using the transition mode of the energy analyzer, where the vertical axis represents the vertical position of irradiated area, and the horizontal axis represent the kinetic energy of the photonemitted electrons. Obviously, the edge of the spectrum in vertical axis shows a blurred part (blue circle) which comes from other regions such like the sample holder, the fixed wires, etc, so we need to exclude these parts and keep the dash-line area before normalizing.

Fig. 4.11(b) shows the normalized energy distribution curve (EDC) and the abscissa is changed into the energy above Fermi level, which can easily determine the position of the vacuum level and derive the value of work function. There are

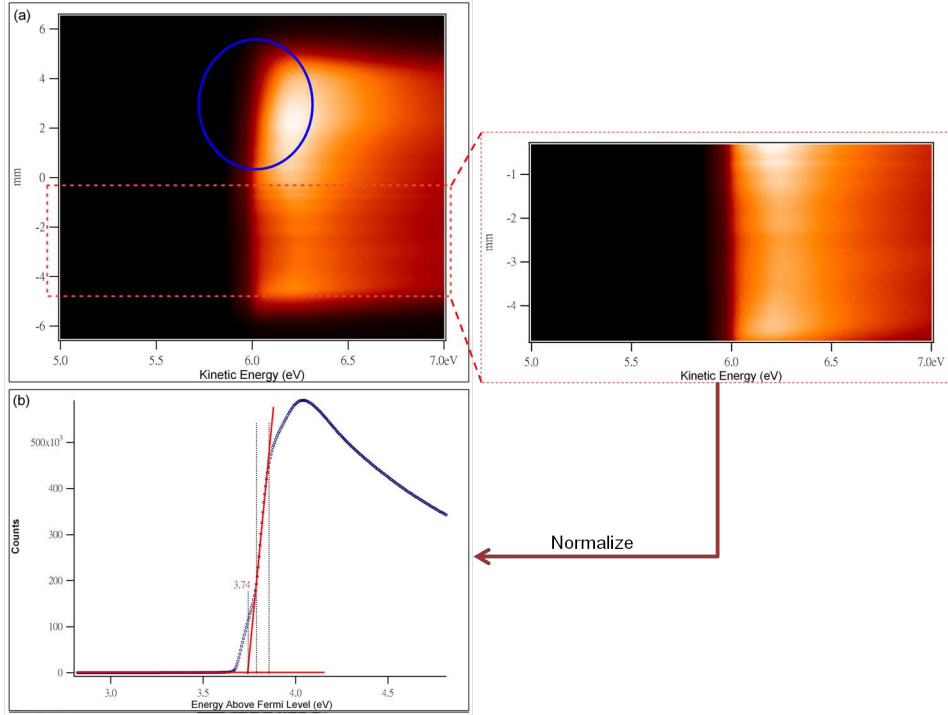


Figure 4.11: (a) The non-normalized cutoff spectrum of 1ML TTC/ 18ML Ag QWS on Ge(111). (b) The normalized energy distribution curve (EDC) from the dash-line region in (a), where the onset of it is defined by the point of intersection between two linear approximation lines.

several different manners to decide the onset of the cutoff spectra. We divided the EDC into three regions and used the linear function to approximate the middle range depicted in Fig. 4.11(b). The intersection of the extended fitting line and energy axis is defined as the position of the cutoff onset.[31]

4.4.2 Results and Comparison

We have measured the work-function changes as a function of TTC thickness by the secondary electron cutoff of the spectra, as exhibited in Fig. 4.12, and the trend is shown in Fig. 4.13. The work function change Δ , was observed on several different substrates, such as 0.3 ± 0.1 (eV) for Pb, 0.5 ± 0.1 (eV) for Ag, and 0.7 ± 0.2 (eV) for Au, respectively.[34] Our measured result shows $\Delta = -0.62$ eV for TTC on Ag thin film. In order to discuss the origin of the vacuum level (VL) shift and the mechanism of the formation of surface dipole layer, some properties of TTC should be emphasized.

TTC ($n\text{-CH}_3(\text{CH}_2)_{42}\text{CH}_3$) is a long-chain normal alkane which has only σ -bonds, and also a typical insulator with a wide gap of about 9 (eV), where charge transfer is not feasible.[35] In addition, n-alkanes are physisorbed on silver surface with small heat of adsorption (6.2 ± 0.2 kJ/mol per CH_2 group)[37], we can expect weak chemical interaction at the interface between TTC and Ag, so that we must consider another mechanism for the formation of surface dipole layer.

From Fig. 4.12, the cutoff shifts significantly to the left by TTC deposition. The maximum of VL shift indicates the coverage of 1 ML due to the formation of the complete surface dipole layer. The value of the work function change observed in our study was -0.62 eV ($\Delta < 0$). The shift of VL by monolayer TTC suggests that the formation of a dipole layer just at the interface. According to the theory of interfacial dipole which was introduced in Sec. 2.4.1, negative value of Δ suggested that the orientation of the surface dipole layer was formed towards the metal substrate, i.e. the electrons accumulated at the interface with the Ag thin films.

4.4.3 Coupling between QWS change and VL shift

There is another interesting issue that the trend of VL shift (Fig. 4.12) is consistent with the shifts of QWS (Fig. 4.8), and we speculated there is some connection between them. The VL shift suggested that the distribution of charge had been changed at the interface between TTC thin films and Ag thin films. On the other hand, the energy shifts of QWS are also related to the phase shift at the interface, which, needless to say, has a lot to do with the charge behavior at the interface. Therefore, the coupling between the VL and QWS shift is expected. In order to ensure the accuracy of this physical phenomenon, we should check whether the similar behavior will be found out in other systems in the future.

4.5 Model

According to the measurement in Ag QWS bands, the occupations of electron density within Ag film decreased due to the existence of TTC molecules. We combined the results of QWS change and VL shift, and proposed a model for this

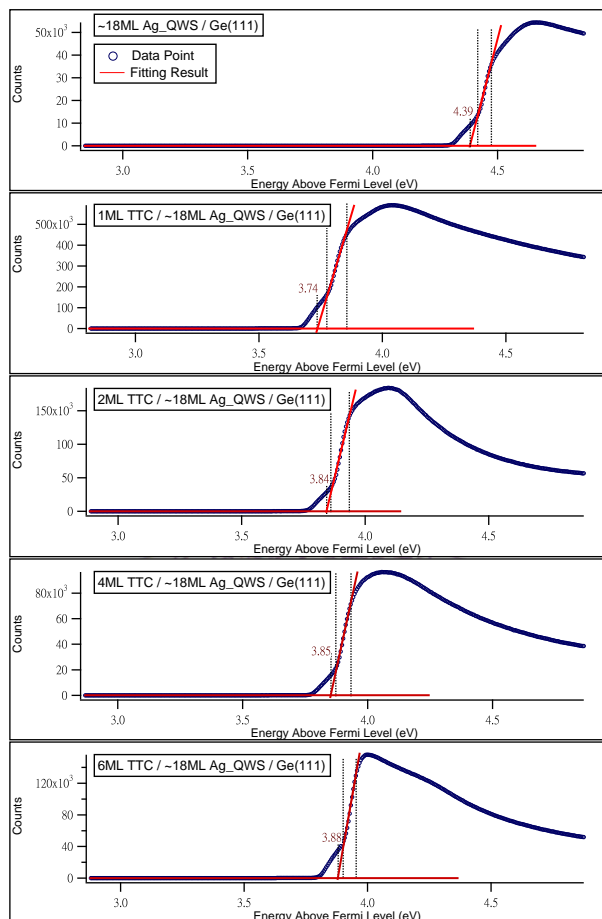


Figure 4.12: The photoemission spectra of the thickness dependence for TTC thin films in cutoff region, and these EDC were taken at 50 eV photon energy, where the abscissa is the binding energy relative to the Fermi level.

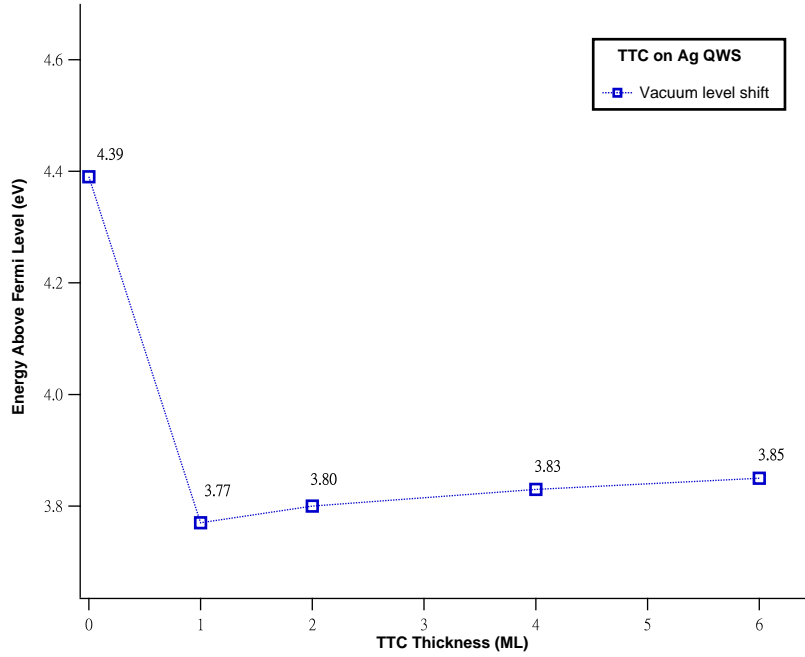


Figure 4.13: Cutoff change of TTC thin films/18 ML Ag/Ge(111), where the abscissa is the thickness of TTC thin film and the vertical coordinate is the energy above the Fermi level. The vacuum level shift Δ is about - 0.62 eV.

TTC/Ag films/Ge(111) system, as shown in Fig. 4.14(d). According to LEED pattern taken for 18 ML Ag films at 55 eV as shown in Fig. 4.14(a), a 1×1 structure was formed on surface for 18 Ag film on Ge(111). The lattice constant of Ag and Ge in (111) direction are $a_{Ag(111)} = 2.89 \text{ \AA}$ and $a_{Ge(111)} = 4.00 \text{ \AA}$, so we can clarify the red and green arrows indicate the spot produced by Ag and Ge atoms, respectively. Analysis of the band dispersions in the range of larger binding energy offers information about their electronic structure as well as the molecular orientation indicates the TTC molecules are parallel to the surface (flat-on orientation) and aligned 60 degrees with each other, as schematically shown in Fig. 4.14(b).

Combing the results of QWS and VL shift, we speculated that the image charge effect takes place to form a surface dipole layer at the interface. The negative charge layer at the TTC side depletes the QWS electrons of Ag films to the Ge(111) substrate, causing the decreased phase shift at the TTC/Ag interface because the phase shift can be regarded as the charge spillage at the interface. The dispersion relations are governed by quantization condition :

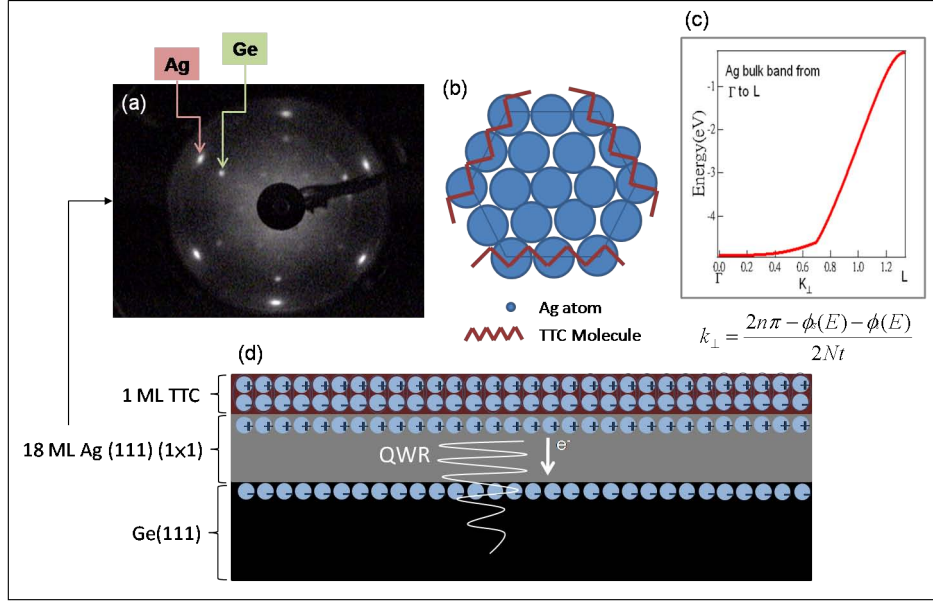


Figure 4.14: (a) LEED pattern taken for 18 ML Ag films at 55 eV. (b) Different orientations of TTC molecules grow on the Ag atoms. (c) Ag bulk band. (d) The model of 1 ML TTC/18 ML Ag/Ge(111) system.

$$k_{\perp} = \frac{2n\pi - \phi_s(E) - \phi_i(E)}{2Nt} \quad (4.2)$$

where k_{\perp} is the wave vector component perpendicular to the film surface, and $\phi_s(E)$ and $\phi_i(E)$ are the energy dependent phase shift of an electron upon reflection at the surface and the interface, respectively. N is the number of Ag monolayer, t is the lattice spacing of Ag in (111) direction, and n is a quantum number.

Due to the decreased phase shift at the TTC/Ag interface, the wave vector component perpendicular to the film surface is increased slightly. From the Ag bulk band shown in Fig. 4.14(c), this increase of wave vector result in the binding energy of QWS decreasing, which is consistent with the QWS energy shift we observed.

Bibliography

- [1] T.-C. Chiang, *Surf. Sci. Rep.* **39**, 181 (2000)
- [2] F. Krok, F. Buatier de Mongeot, M. Goryl, J. J. Kolodziej, and M. Szymonski, *Phys. Rev. B* **81**, 235414 (2010)
- [3] S.-J. Tang, W.-K. Chang, Y.-M. Chiu, H.-Y. Chen, C.-M. Cheng, and K.-D. Tsuei, *Phys. Rev. B* **78**, 245407 (2008)
- [4] S.-J. Tang, T. Miller, and T.-C. Chiang, *Phys. Rev. Lett.* **96**, 036802 (2006)
- [5] H. Ishii, K. Sugiyama, E. Ito, and K. Seki, *Adv. Mater.* **11**, 605 (1999)
- [6] H. Ishii, E. Morikawa, S. J. Tang, D. Yoshimura, E. Ito, K. Okudaira, T. Miyamae, S. Hasegawa, P. T. Sprunger, N. Ueno, K. Seki, and V. Saile, *J. Electron Spectrosc. Relat. Phenom.* **101 – 103**, 559-564 (1999)
- [7] Charles Kittel, *Introduction to Solid State Physics*, J. Wiley
- [8] Hans Lüth, *Surfaces and Interfaces of Solid Materials*, Springer
- [9] Stefan Hüfner, *Photoelectron Spectroscopy*, Springer
- [10] H. Hertz, *Ann. Physik* **31**, 983 (1887) Springer
- [11] I. Razado-Colambo, Jiangping He, H. M. Zhang, G. V. Hansson, and R. I. G. Uhrberg *Phys. Rev. B* **75**, 205410 (2009)
- [12] M. Abe, Y. Sugimoto, S. Morita *Nanotechnology* **16**, S68-S72 (2005)
- [13] J. A. Venables, *Introduction to Surface and Thin Film Process*, Cambridge University Press, Cambridge, United Kingdom, 2001
- [14] *User Manual SCIENTA R3000*, VG SCIENTA

- [15] *User Manual SPECTRALEED* , Omicron
- [16] *Operating Manual and Programming Reference*, Stanford Research Systems
- [17] Andrew Zangwill, *Physics at Surfaces*
- [18] M. H. Upton, *Photoemission Studies of the Electronic Structure and Properties of Thin Lead Films*, *Ph.D. Thesis* University of Illinois at Urbana-Champaign, 2005
- [19] D. A. Ricci, *Photoemission Studies of interface effects on thin film properties*, *Ph.D. Thesis* University of Illinois at Urbana-Champaign, 2006
- [20] J. Schwinger *Phys. Rev.* **75**, 1912 (1949)
- [21] <http://www.srrc.gov.tw/>
- [22] John F. Watts, John Wolstenholme, *An Introduction to Surface Analysis by XPS and AES (1st ed.)* Chichester, West Sussex, England ; New York : J. Wiley
- [23] E. W. Plummer, W. Eberhardt, *Angle-Resolved Photoemission as a Tool For The Study of Surfaces*
- [24] A. L. Wachs, T. Miller, T. C. Hsieh, A. P. Shapiro, and T.-C. Chang, *Phys. Rev. B* **32**, 2326 (1985)
- [25] K. Kanai, Y. Ouchi, K. Seki, *Thin Solid Films* **517**, 3276-3280 (2009)
- [26] F. Patthey, J.-M. Imer, W.-D. Schneider, H. Beck, and Y. Baer, *Phys. Rev. B* **42**, 8864 (1990)
- [27] René Matzdorf, *Investigation of Line Shapes and Line Intensities by High-resolution UV-photoemission Spectroscopy - Some Case Studies on Nobel-metal Surface*, Elsevier
- [28] Andrea Damascelli, *Physica Scripta.* **T109** (2004)
- [29] S.K. Mahatha, S.R. Menon, *Current Science Vol. 98, no.6* ,759 (2010)
- [30] D. Cahen, A. Kahn, *Adv. Mater.* **15**, 271 (2003)
- [31] D. Yoshimura, H. Ishii, Y. Ouchi, E. Ito, T. Miyamae, S. Hasegawa, K. Okudaira, N. Ueno, and K. Seki, *Phys. Rev. B* **60**, 9046 (1999)

- [32] D. Yoshimura, H. Ishii, Y. Ouchi, E. Ito, T. Miyamae, S. Hasegawa, N. Ueno, and K. Seki, *J. Electron Spectrosc. Relat. Phenom.* **88 – 91**, 875 (1998)
- [33] David J. Willock, *Molecular Symmetry*, Wiley
- [34] E. Ito, H. Oji, H. Ishii, K. Oichi, Y. Ouchi and K. Seki, *Chem. Phys. Lett.* **287**, 137 (1998)
- [35] K. Seki, E. Ito, and H. Ishii, *Synth. Metals* **91**, 137 (1997)
- [36] K. Seki, N. Ueno, U. O. Karlson, R. Engelhardt, and E. E. Koch, *Chem. Phys.* **105**, 247 (1986)
- [37] S.M. Wetterer, D.J. Lavrich, T. Cummings, S.L. Bernasek, and G. Scoles, *J. Phys. Chem. B* **102**, 9266 (1998)

